J. Fluid Mech. (1992), *vol.* 235, *pp.* 179–221
Printed in Great Britain

Particle dispersion in the developing free shear layer. Part 2. Forced flow

By B. J. LÁZARO AND J. C. LASHERAS
Department of Applied Mechanics and Engineering Sciences, University of California, San Diego, La Jolla, CA 92093-0411, USA

(Received 27 April 1990 and in revised form 9 March 1991)

In this study we analyse the dispersion mechanisms of small water particles in an acoustically forced plane, turbulent mixing layer. When compared to the naturally developing flow, the excited mixing layer is shown to exhibit drastic changes in the cross-stream particle concentration evolution, with the particles now dispersing laterally at larger rates than that of the longitudinal momentum of the turbulent gas glow. The particle dispersion is shown to occur as a size-selective process characterized by the existence of an intermediate particle size range for which the lateral dispersion is maximized. Unlike in the natural flow evolution, the forced shear layer does not possess a non-dimensionalization rendering particle size independent dispersion properties. It is demonstrated that this behaviour results from the non-similarity of the developing gas motion. The mixing layer is shown to have inhomogeneities both in the droplet concentration and in the droplet-size probability density distribution function. Instantaneous flow visualizations as well as spectral analysis of laser extinction measurements show the presence of a coherent organization in the particle concentration field resulting from the large-scale eddies characterizing the underlying turbulent gas flow. Conditional, phase-average sample techniques are used to analyse the structure of this coherent particle dispersion field. The dispersion is shown to be controlled by an array of large streaks that emanate from the undisturbed spray, engulfing areas which are almost depleted of droplets. The data from the conditional sampling measurements are in good agreement with preliminary results from a simplified Eulerian model of the particle motion, showing the potential that this formulation can have for analysing this type of flow.

1. Introduction

The flow characteristics of the developing mixing layer can be substantially altered by adding a small two-dimensional perturbation to the vorticity shed from the splitter plate. For a single-wave periodic perturbation with frequency within the unstable shear-layer range, the evolution of the flow is characterized by the rapid growth of the Kelvin–Helmholtz instability, leading to the formation of a row of large spanwise vortices of equal circulation and uniformly spaced. These spanwise vortices persist several wavelengths before undergoing interactions with each other. The resulting mixing layer is characterized by growth rates that differ appreciably from those found in the naturally developing case. In addition, the evolution of the flow towards an asymptotic, self-similar state is significantly delayed (Ho & Huang 1982).

In the forced shear layer, the dispersion of particles of a given size is largely dictated by their interaction with the velocity fluctuations associated with the

dominant flow scale. As was shown to occur in the unperturbed mixing layer, substantial changes in the particle dispersion properties should be expected as one moves downstream. In the present flow, however, the long lifetimes of the spanwise vortices gives rise to distinct particle dispersion characteristics. Also, the highly organized particle response to the coherent velocity field allows a detailed study of their dispersion, thus providing basic information for modelling flows in which multiple coherent scales are present.

The present investigation, therefore, explores the effect of a dominant, single flow scale on the particle dispersion process. It complements the experiments reported in the unforced mixing layer which were characterized by the presence of a wide range of spanwise vortical scales at every downstream location (see Part 1, Lázaro & Lasheras 1992). In the present work we restrict ourselves to a description of the evolution of the flow in the developing region along which vortex interaction effects such as pairing or amalgamations do not occur. Moreover, in order to be able to obtain a detailed internal structure of the particle dispersion field, only one frequency of excitation is investigated. However, limited preliminary flow visualizations showing the effect of the forcing frequency on the dispersion process are also presented.

This second part is presented in the same way as was the study of the natural flow field (Part 1). First, the experimental modifications necessary to perform the forced studies are briefly described. Second, the main characteristics of the longitudinal gas velocity field are introduced. Next, a discussion of the mean particle dispersion properties is followed by a description of its fluctuating temporal structure. Then an analysis of forcing signal-phase-conditioned measurements is presented. Finally, an Eulerian study of the particle dispersion problem in a simplified gas flow field is discussed and the results are compared with the experimental findings.

2. Experimental conditions

The flow facility used in the natural flow study (Part 1) was modified to allow for the forcing of the primary instability in the shear layer. The technique used is similar to the one developed by Fiedler & Mensing (1985). The forcing device consists of a loudspeaker placed on top of a small air chamber located in the stagnant air side of the mixing layer (figure 1). The chamber's only aperture is a small slit parallel to the trailing edge of the splitter plate. The oscillation of the speaker membrane is transformed into a vertical velocity perturbation in the base-flow boundary-layer velocity profile issuing from the plate. The loudspeaker is fed with a pure sinusoidal wave produced by a signal generator and a low-noise audio amplifier. The amplitude of the perturbation is adjusted to quickly saturate the growth of the shear-layer instability at the forcing frequency.

For comparison, the selected free-stream values of the longitudinal gas velocity, the particle concentration and the particle volume-size distribution function were the same used in the natural gas, namely $\bar{u}_{g\infty} = 15\ \mathrm{ms}^{-1}$ and $\bar{\alpha}_{p\infty} = 1.6 \times 10^{-5}$. The addition of the coherent perturbation resulted in no significant changes in the longitudinal mean and fluctuating velocity profiles at the end of the splitter plate ($x = 0$) compared with the natural flow. Therefore, the initial profiles of $\bar{u}_g$, u'_g, the overall particle concentration ($\bar{\alpha}_p$) and the particle volume-size distribution function ($f(D)$) were identical to the ones measured in the naturally developing flow, presented in figures 4, 5 and 6 in Part 1.

As was the case with the natural flow, the experimental characterization of the gas

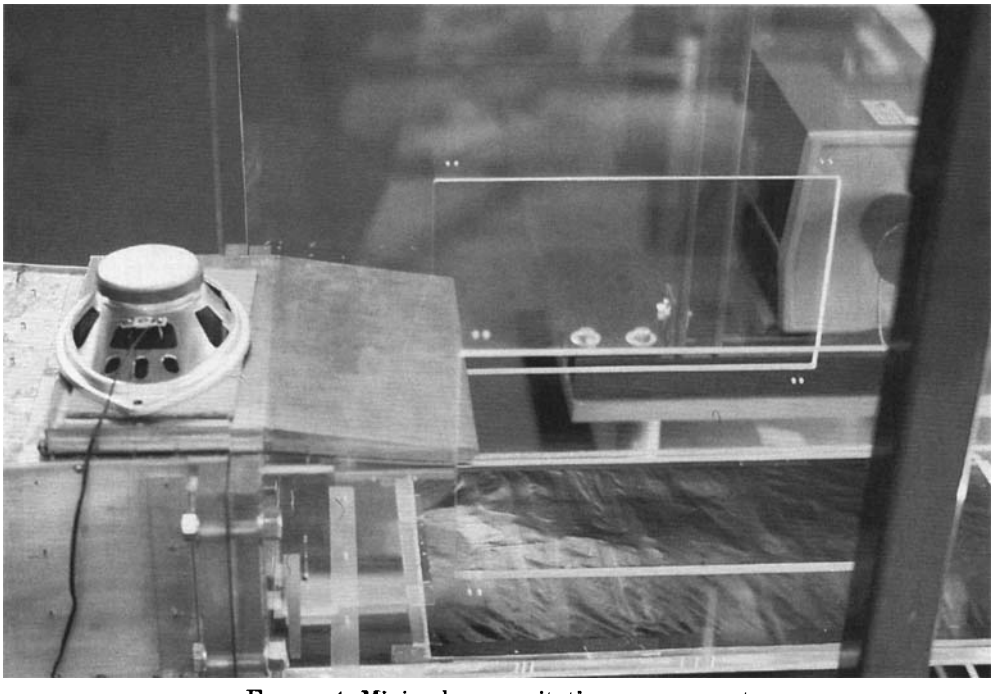

FIGURE 1. Mixing-layer excitation arrangement.

motion was achieved by measuring the longitudinal gas velocity with a single Pt–10%Rh hot wire. An obscuration probe and a small-angle diffraction Malvern particle sizer were used to measure the evolution of the spray concentration and volume-size distribution function. Details of the measuring techniques are given in part 1.

In addition to the signal processing techniques employed in the natural case, conditional phase-average measurements were also conducted in the present study. Conditional sampling has already proven to be a useful tool for extracting information about some of the relevant mechanisms characterizing turbulent shear flows (Browand & Weidman 1976; Antonia 1983). Since the shear-layer instability quickly saturated the forcing frequency, we have used conditional phase-averaged measurements to characterize the role of the large-scale eddy structure in the particle dispersion process. For the longitudinal gas velocity and laser attenuation measurements the conditional sampling was performed via software. A multichannel data logger was used to acquire the output signals from the hot wire, the obscuration probe and the function generator simultaneously. The forcing waveform was then used to sort the gas velocity and laser attenuation signals into 36 intervals covering the phase range $[0, 2\pi]$. The conditional measurements involved averaging over 560 forcing cycles, which resulted in an estimated 0.4% statistical error. The phase-average measurements for the particle sizer involved the design of a trigger unit that generated a set of TTL pulses having a given, variable phase delay with respect to the mixing-layer excitation waveform. In order to minimize errors in the phase delay, the forcing function was also generated from the trigger unit clock using an EPROM microchip and an 8 bits D/A converter. The TTL pulses were then used to trigger the Malvern particle sizer. In this case, the conditional measurements involved averaging over 200 forcing cycles and the total phase range was divided into

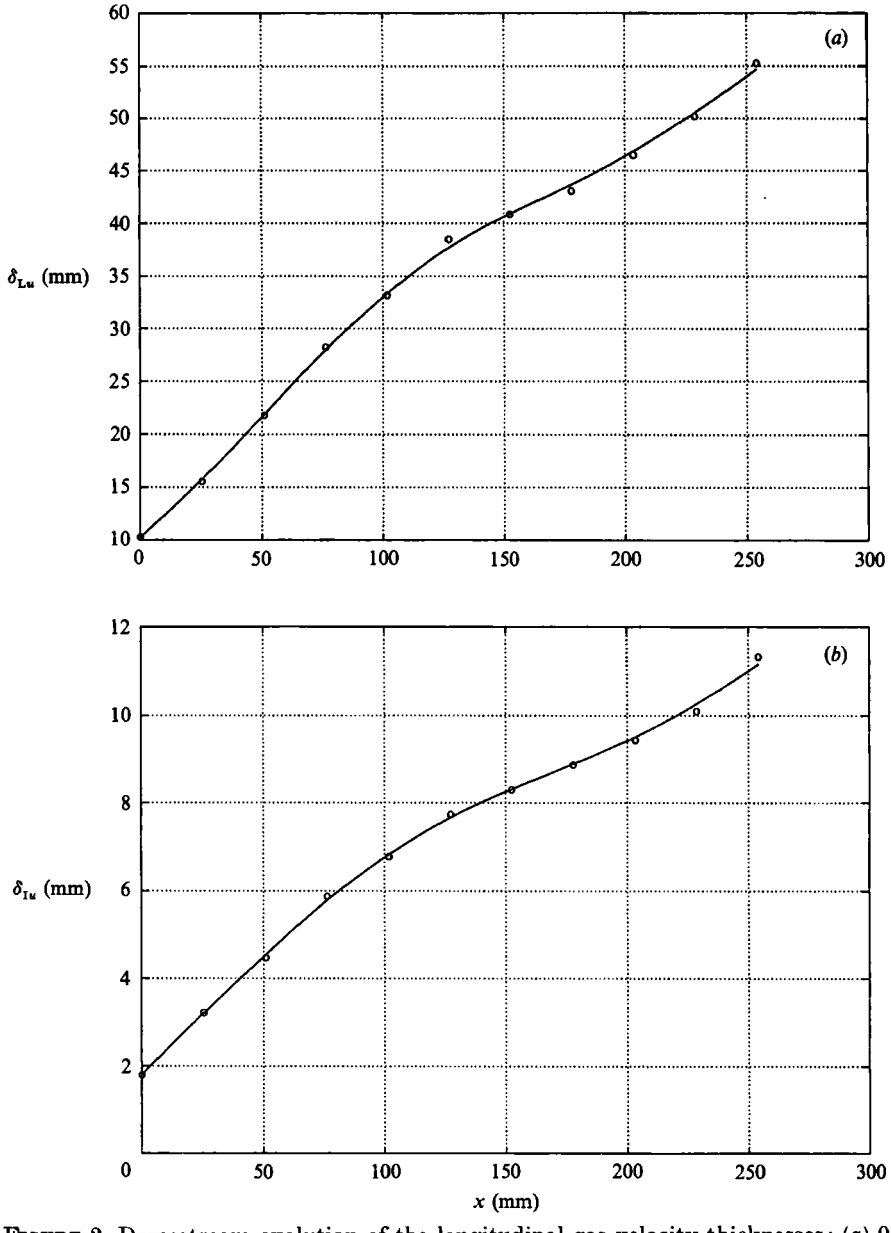

FIGURE 2. Downstream evolution of the longitudinal gas velocity thicknesses: (*a*) 0.1–0.9 level thickness, (*b*) integral (momentum) thickness.

32 intervals. Details of the design and construction of the trigger unit can be found in Lázaro (1989).

All the measurements reported in this Part were obtained by forcing the mixing layer with an excitation frequency $f_f = 72$ Hz. This frequency is close to the subharmonic of the initially most amplified perturbation found in the natural flow evolution (Part 1). In addition, flow visualizations of the particle dispersion field with the mixing layer forced at $f_f = 140$ Hz were obtained to provide qualitative information about the effect of the forcing frequency on the dispersion of the particulate.

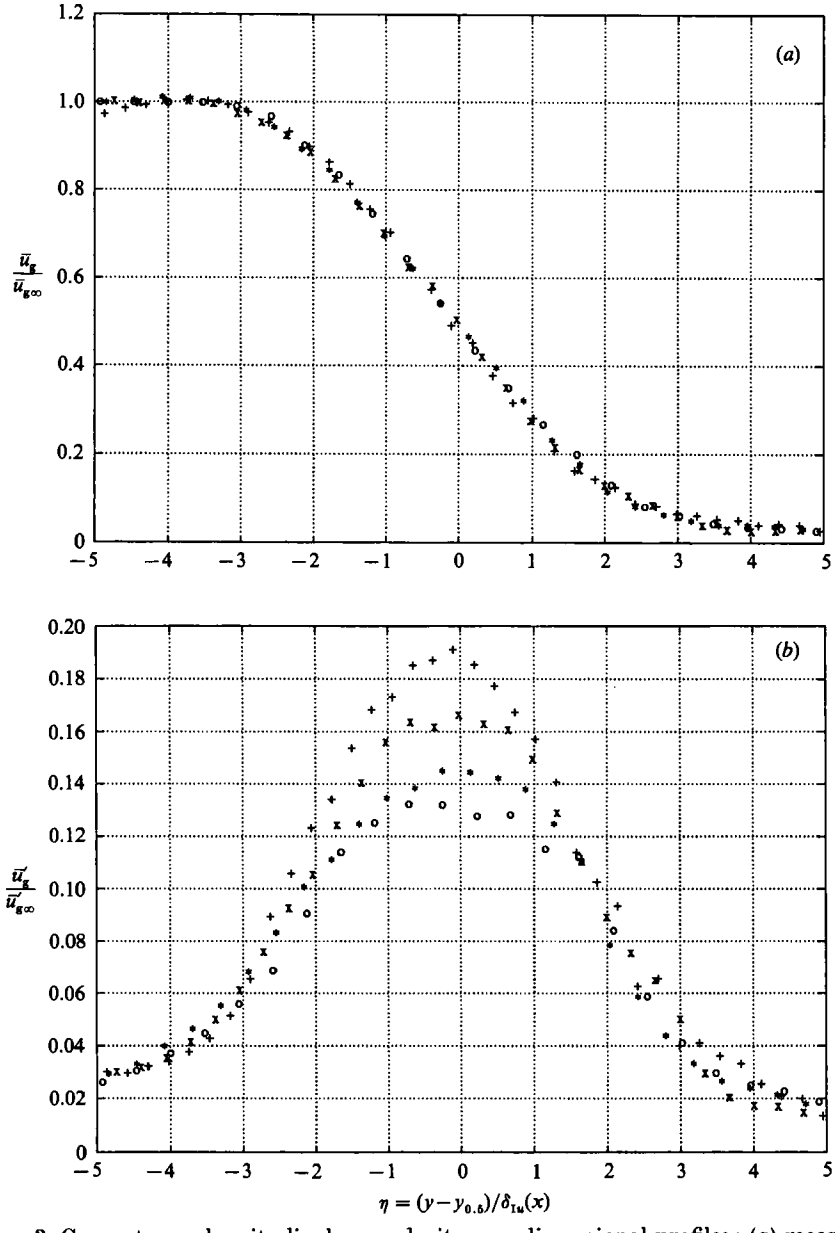

FIGURE 3. Cross-stream longitudinal gas velocity non-dimensional profiles: (*a*) mean velocity, (*b*) r.m.s. velocity. Cross-stream coordinate non-dimensionalized with the local momentum thickness. ○, $x = 10.2$ cm; *, 15.2 cm; ×, 20.3 cm; +, 25.4 cm.

3. Longitudinal gas velocity field

The highly nonlinear character of the flow development in the excited shear layer can be observed in the downstream evolution of the mixing-layer thicknesses shown in figure 2(*a*) (0.9–0.1 level thickness) and 2(*b*) (integral thickness). Note that the growth rates are first seen to slowly decrease until a downstream distance of $x = 17.5$ cm is reached, where an inflexion point is located. From there on, the thicknesses show increasing growth rates up to the furthest x positions measured.

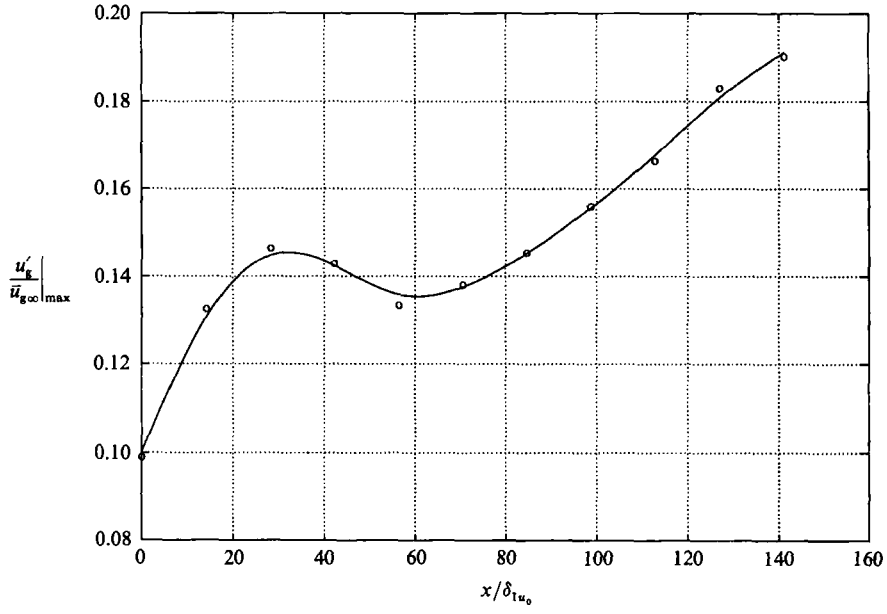

FIGURE 4. Downstream evolution of the maximum r.m.s. value of the fluctuating carrier gas longitudinal velocity.

When the non-dimensional mean velocity profiles are plotted against $\eta = y - y_{0.5}/\delta_{Iu}(x)$, figure 3(*a*), the data are found to collapse onto a single curve. As a consequence, and as a result of the nonlinear growth of $\delta_{Iu}(x)$, the forced mixing layer lacks the type of relationship $\bar{u}_g = \bar{u}_g(y/x)$ shown in Part 1 to hold as a good approximation in the natural case.

The degree of equilibrium in the fluctuating velocity r.m.s. profiles is shown in figure 3(*b*). A substantial amount of flow development is still present at the farthest location measured, $x = 25.4$ cm. Approximately, the peak in the r.m.s. profile is located along the line $\eta = 0$, exhibiting levels considerably higher than the ones found in the natural case. The evolution of the r.m.s. peak value with the downstream location is shown in figure 4. The saturation of the forcing mode is essentially completed at $x/\delta_{Iu_0} = 42$. The r.m.s. peak profile also shows the typical relaxation that takes place once saturation has been reached (Freymuth 1966). In parallel, the significant growth of additional modes present in the initial turbulent boundary layer can be seen to occur in the more advanced stages of flow development.

A typical plot of the spectral content of the velocity fluctuations is shown in figure 5. The peak corresponding to the excitation frequency appears 30 dB above the spectral baseline. The streamwise position selected ($x/\delta_{Iu_0} = 105$), is, as shown in figure 4, downstream of the location where the saturation of the forcing mode occurs. Also, the progressive activity of turbulent low-frequency fluctuations can be noticed emerging to the left of the coherent peak. Eventually the interaction between these low-frequency modes and the coherent peak leads to the pairing of two consecutive vortices. However, no clear spectral evidence of this interaction process could be found in the present measurement window.

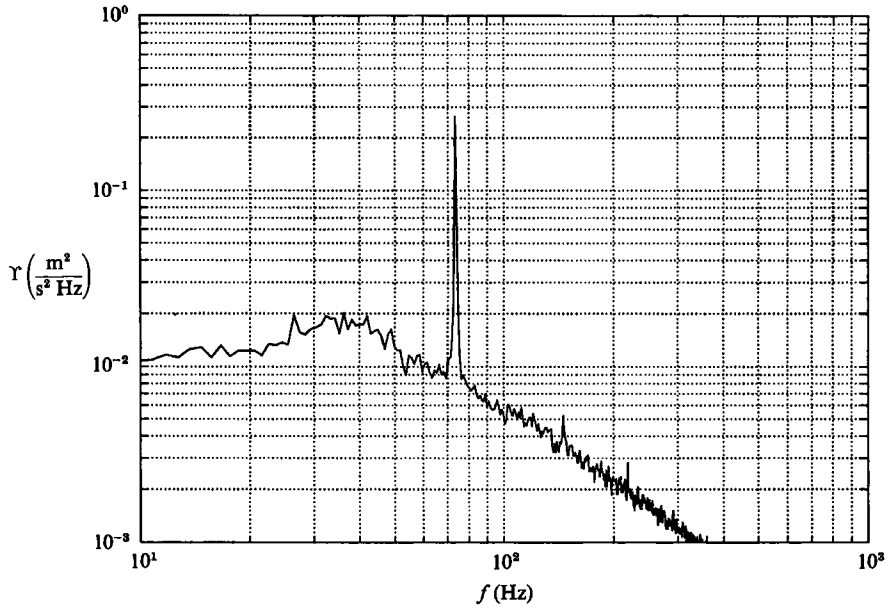

FIGURE 5. Longitudinal gas velocity power spectrum, $x = 17.8$ cm, $y = -12.7$ mm.

4. Mean particle dispersion characterization

Long-time-exposure photographs showing the global characteristics of the particle dispersion process for two different forcing frequencies, $f_f = 72$ and 140 Hz, are shown in figures 6(*a*) and 6(*b*), respectively. The selected frequencies are close to the initial most unstable one measured in the natural flow (136 Hz) and its first subharmonic respectively (Part 1). These flow visualizations, when compared with the one obtained for the natural flow (figure 11 in Part 1), reveal the enhanced particle dispersion properties of the excited mixing layer. Note that the increase of the particulate's spreading angle is dramatic, especially when the mixing layer is forced with the subharmonic frequency. The outer edge of the dispersion layer is characterized by a nonlinear shape, noticeable in the initial region of flow development (left portion of figure 6*a*). In addition, when the mixing layer is forced with the initial most unstable frequency, figure 6(*b*), curvature changes in this outer edge are also seen to occur farther downstream. It is interesting to note that the forced dispersion layers show a large degree of intensity inhomogeneity even in the long-time-exposure flow visualizations. This effect is particularly visible in the subharmonic forcing. In this case, and soon after the trailing edge of the splitter plate, the dispersion layer exhibits two well-differentiated regions. The upper, external portion shows a divergent shape and is characterized by an enhanced particle scattering intensity. The internal region, running almost parallel to the streamwise direction, exhibits considerably lower light-scattering intensity levels. When the mixing layer is forced with its most unstable frequency, the same spatial organization is seen to appear in the leftmost part of the dispersion region (figure 6*a*). Observe the band of reduced light-scattering intensity running parallel to the inner edge of the dispersion layer, which eventually disappears at about 30% of the downstream length shown in the photograph. These observations point out the scale relationship existing between the particle responses at the two excitation frequencies shown, i.e. one could expect that a close-up view of the initial dispersion layer in figure 6(*b*) shall be analogous to the visualization shown in figure 6(*a*).

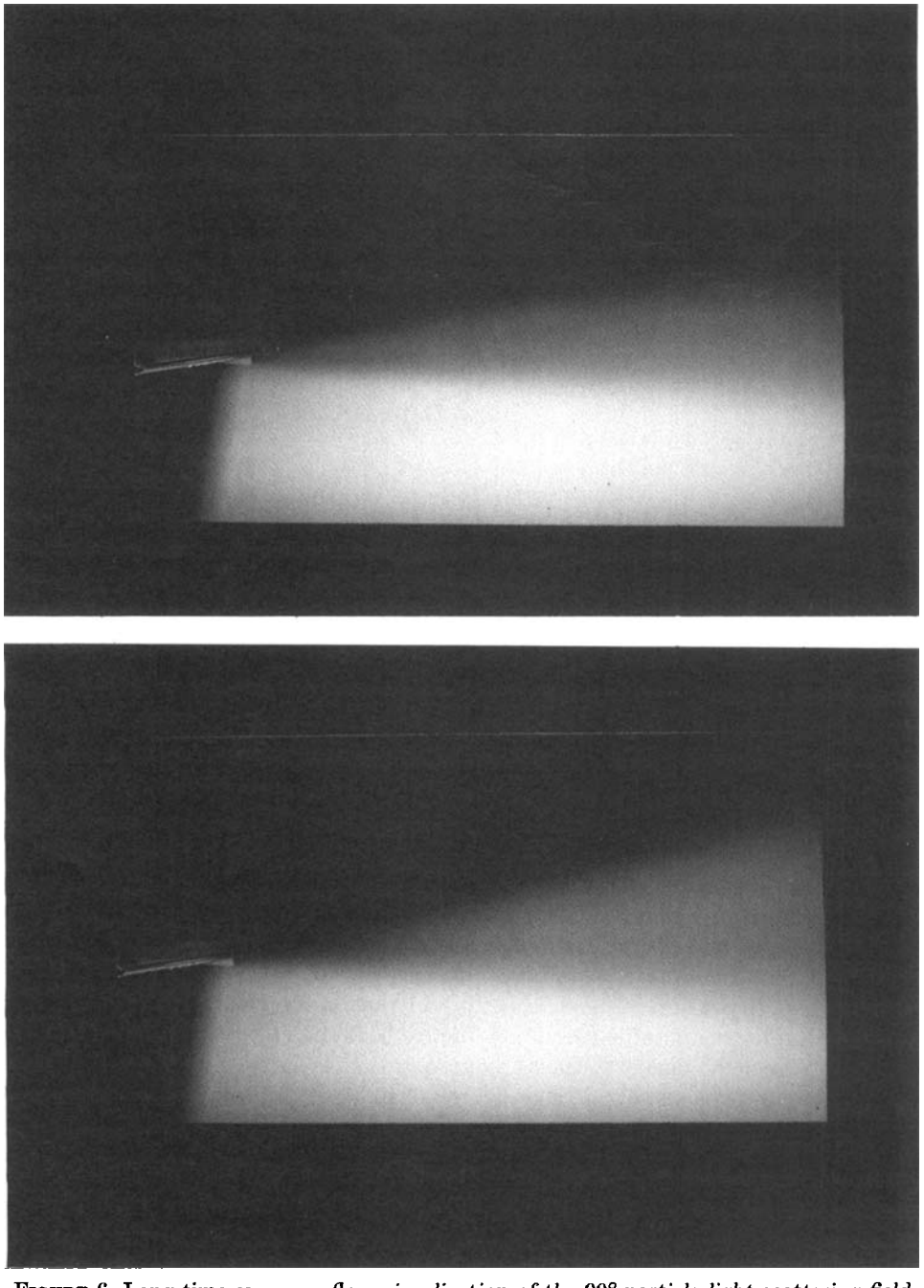

FIGURE 6. Long-time-exposure flow visualization of the 90° particle light scattering field. Forcing frequency (a) $f_f = 72$ Hz, (b) $f_f = 140$ Hz.

The non-dimensional particle concentration evolution for the mixing layer forced with the subharmonic frequency ($f_f = 72$ Hz, the frequency used in all the measurements presented hereafter) is shown in figure 7. Notice that the asymmetry of the profiles, already shown to exist in the natural flow, has become more acute in the forced dispersion layer. In addition, the mean particle concentration is found to

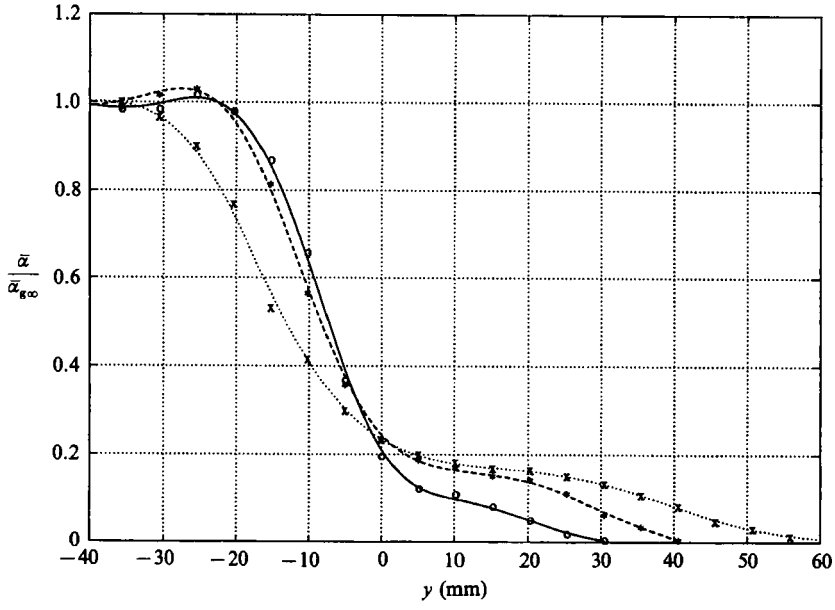

FIGURE 7. Cross-stream profiles of the mean overall particle concentration: ○, $x = 10.2$ cm; *, 15.2 cm; ×, 25.4 cm.

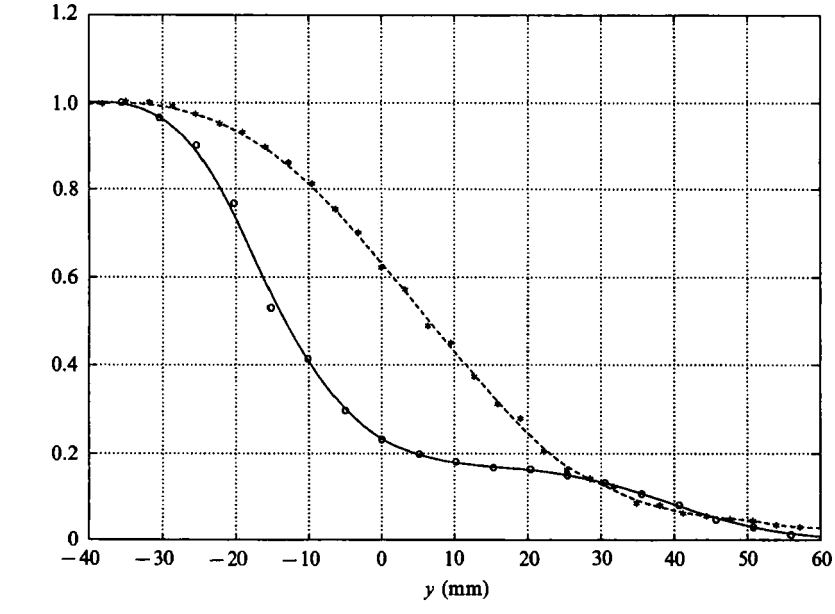

FIGURE 8. Comparison of the cross-stream profiles of the mean carrier gas velocity (*) and overall particle concentration (○) at $x = 25.4$ cm.

be characterized by a triple-inflexional profile exhibiting severe curvature changes. As one moves from the core of the spray to the external regions of the dispersion layer, an initial, strong concentration decay is followed by a region in which the profile stabilizes, creating a plateau zone that covers the central portion of the dispersion layer. The extension of the plateau region increases with the downstream

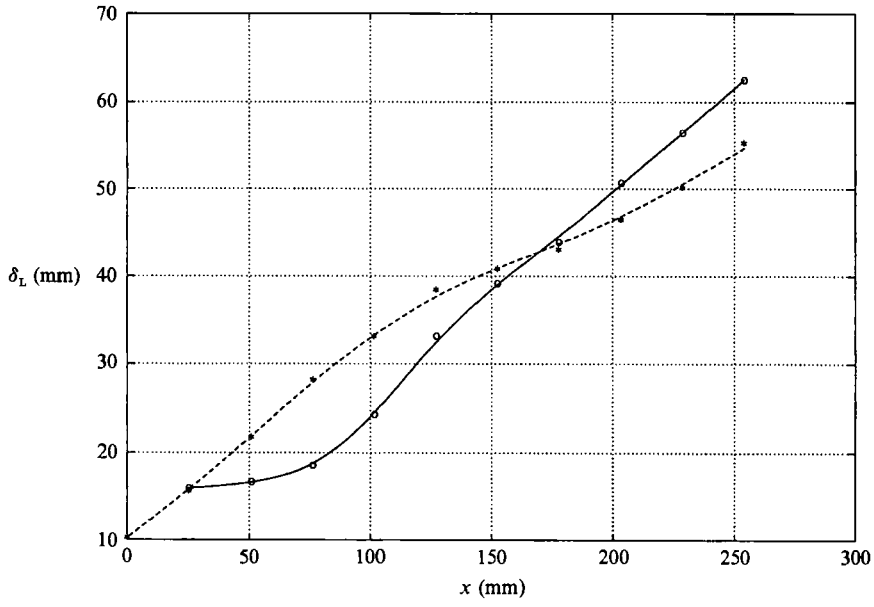

FIGURE 9. Overall particle concentration 0.1–0.9 level thickness (○). The evolution of the carrier gas longitudinal velocity level thickness (*) is also shown for comparison.

location. The plateau is followed by a third region where the concentration slowly decays to reach its background level (zero value). These measurements are consistent with the flow visualizations discussed above, with the plateau region corresponding to the central region of reduced scattering intensity in figure 6(*b*). Since the concentration profile is, in fact, strictly monotonic, one can infer that an accumulation of small particulate must be taking place in the intermediate zones of the dispersion layer.

A comparison between the mean particle concentration and velocity profiles (figure 8) reveals that, in the external regions of the mixing layer, the stabilization effect that generates the plateau region causes the concentration profile to overshoot that of the longitudinal gas momentum. In addition, the large cross-stream extension of the particle concentration profile results in a much faster decay in the inner edge of the dispersion layer. Both effects generate a dramatic change in the dispersion properties as compared with the naturally developing mixing layer. To visualize this point, a comparison between the 0.1–0.9 level thickness of the particle concentration ($\delta_{L\alpha}$) and gas velocity (δ_{Lu}) profiles is shown in figure 9. Recall that for the naturally developing mixing layer, owing to the presence of the initial induction region, the concentration thicknesses were always lagging well behind those of the velocity (Part 1). The forced case also shows the presence of an induction region characterized by a positive curvature. However, this region now spans along a shorter distance than the one found for the natural case, and furthermore it ends with a spectacular increase in the growth rate. As a result, the more advanced downstream locations exhibit concentration thicknesses surpassing the corresponding quantities defined for the gas velocity profiles.

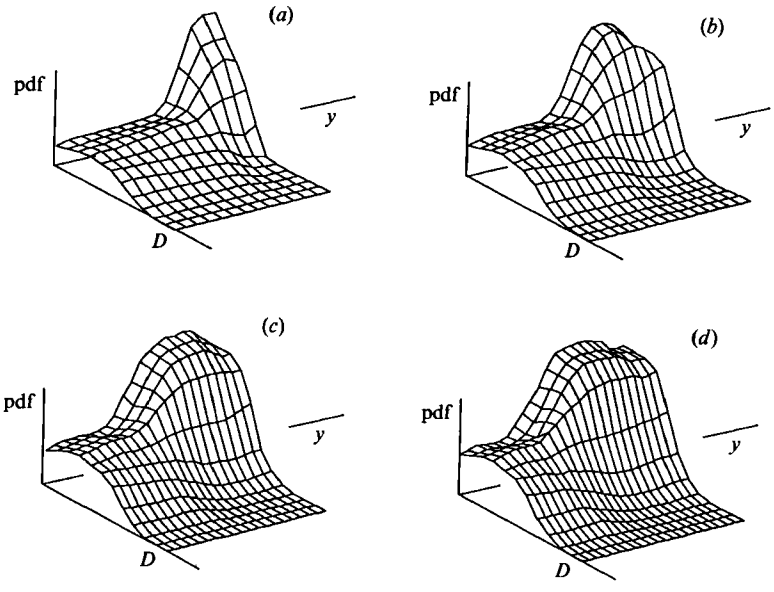

FIGURE 10. Downstream evolution of the mean particle volume-size probability density function. Each plot represents the cross-stream variation at a given x. (*a*) $x = 7.6$ cm, (*b*) 12.7 cm, (*c*) 20.3 cm, (*d*) 25.4 cm.

5. Particle size effects in the forced dispersion layer

The particle density distribution functions obtained in the forced mixing layer (figure 10) bear an extensive resemblance to the ones found in the naturally developing flow. The most relevant characteristic of the mixing region is, again, the strong selective action that it exhibits with respect to the small droplets. Also, as was the case with the natural flow, local changes in the probability density function (p.d.f.) can be identified in the outer edge of the dispersion region. This external sublayer is characterized by a local reduction of the small droplets and the corresponding increase in the p.d.f. percentages of the large ones. The threshold diameter for this external sublayer almost coincides with the one for which the selective dispersion action occurs. Finally, the higher-x-locations surfaces also show the presence of an internal sublayer which emerges as a small bump in the tail of the large-diameter p.d.f.

In the p.d.f. plots corresponding to large values of the downstream coordinate ($x = 20.3$ cm and especially $x = 25.4$ cm), the central zone of the dispersion layer exhibits very small changes in the probability density percentages. Therefore, one can divide the mixing region into three. Moving from the core of the spray outward along the y-coordinate, in the first region the small droplets increase their p.d.f. value at the expense of a reduction in the percentage of the large-diameter groups; in the second region, the p.d.f. is approximately frozen and no substantial changes are seen to occur; finally, in the third, outer area, the large droplets show an increase in their p.d.f. percentage. This pattern suggests the existence of several competing events whose relative weights are responsible for the measured time-average distribution function.

A comparison between the downstream evolution of the p.d.f. percentage for two distinct particle sizes, non-dimensionalized by their free-stream values, is given in figure 11. The frozen p.d.f. region is hardly distinguishable in the early downstream

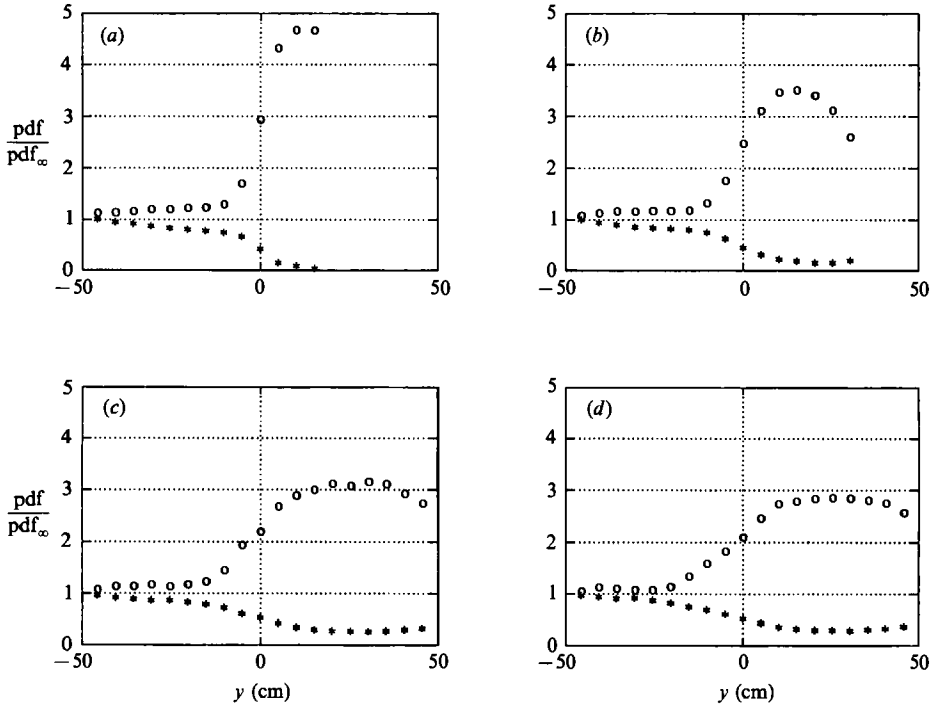

FIGURE 11. Downstream evolution of the droplet p.d.f. for particle size groups, ○, $\bar{D} = 13.0$ μm; and *, $\bar{D} = 57.4$ μm. (a) $x = 7.6$ cm, (b) $x = 12.7$ cm, (c) $x = 20.3$ cm, (d) $x = 25.4$ cm.

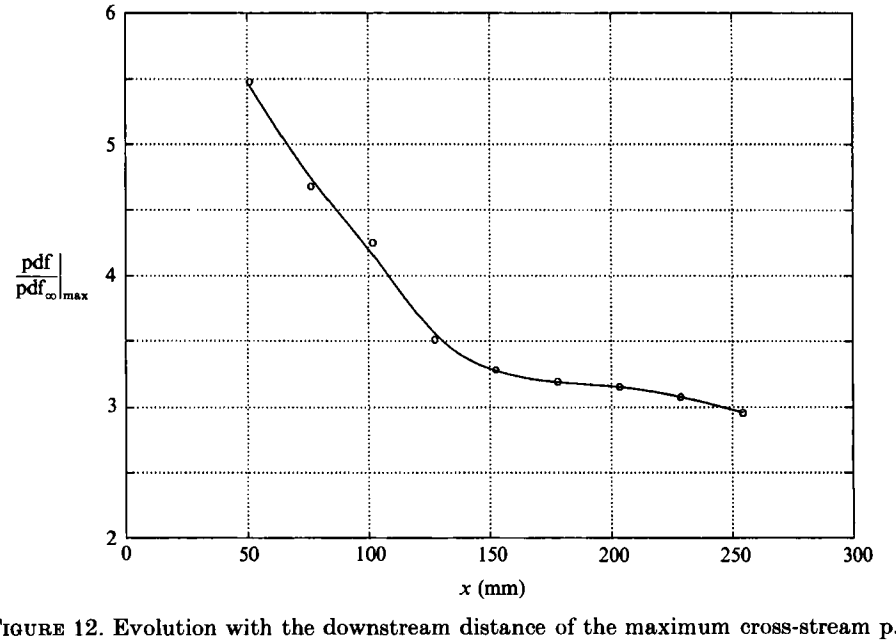

FIGURE 12. Evolution with the downstream distance of the maximum cross-stream p.d.f. value for the $\bar{d} = 13$ μm size group.

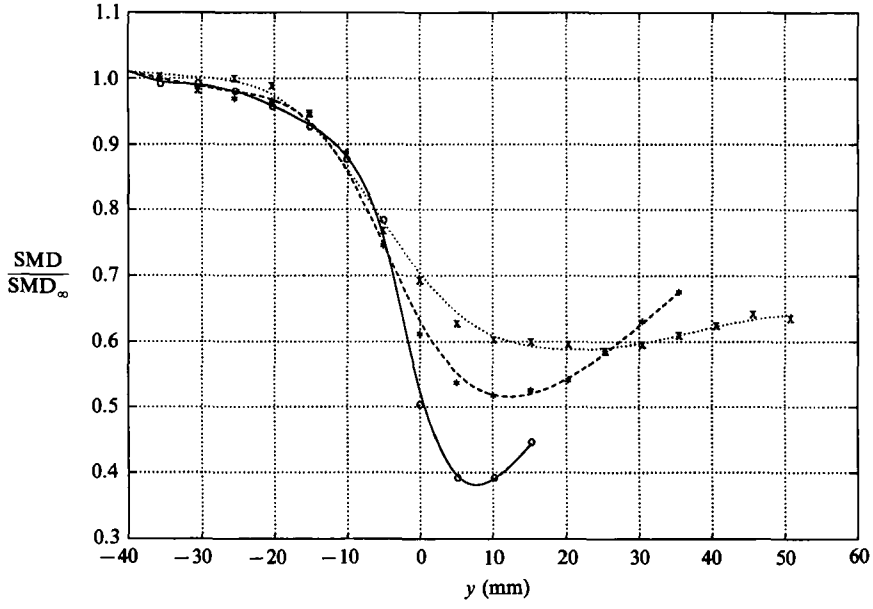

FIGURE 13. Cross-stream profiles of the mean Sauter mean diameter of the particle size distribution: ○, $x = 5.1$ cm; *, 12.7 cm; ×, 20.3 cm.

locations, becomes apparent at $x = 20.3$ cm and especially visible at $x = 25.4$ cm. Therefore, it takes some flow flight time until the p.d.f. stabilization effect shows up. Also noticeable in this figure is the tendency of the dispersion layer to reach the p.d.f. values characterizing the free-stream spray. In an ideal, size-independent dispersion situation, the curves of figure 11 would be straight lines at level 1. The relaxation towards this size-independent state occurs first at a fast rate ($x = 7.6$ to 20.3 cm). However, notice that the process slows down once the emergence of the frozen p.d.f. region has occurred in the central dispersion layer. This change in the homogeneization tendency is more apparent in figure 12, which presents the downstream evolution of the cross-stream peak value in the p.d.f. percentage for $\bar{D} = 13$ μm. Notice that a sudden change in the decay pattern occurs at $x = 15$ cm. Since this downstream position is situated around the location for which the stabilized p.d.f. region starts to emerge, a link between the two phenomena seems to exist. In addition, both appear to be the result of a localized event.

Cross-stream profiles of the temporal mean of the Sauter mean diameter (SMD) measured at different downstream positions are shown in figure 13. The intermediate plot, $x = 12.7$ cm, is located immediately upstream of the change in the homogeneization pattern described above. Upstream of this point, the external regions of the dispersion layer show a continuous increase in the SMD values. On the other hand, further downstream, an equalization in the mean diameter occurs. In addition, the formation of the internal sublayer is also appreciable in the $x = 20.3$ cm graph, as a region of local SMD increase that appears to balance the sedimentation process occurring in the cross-stream locations $-30 < y < 20$ mm.

Information on the relative extension of the dispersion process for different particle sizes can be extracted from figure 14. The enhanced presence of small-diameter droplets ($\bar{D} = 16$ and 27 μm) in the dispersion layer can be identified with two well-defined characteristics of the concentration profiles for different particle sizes:

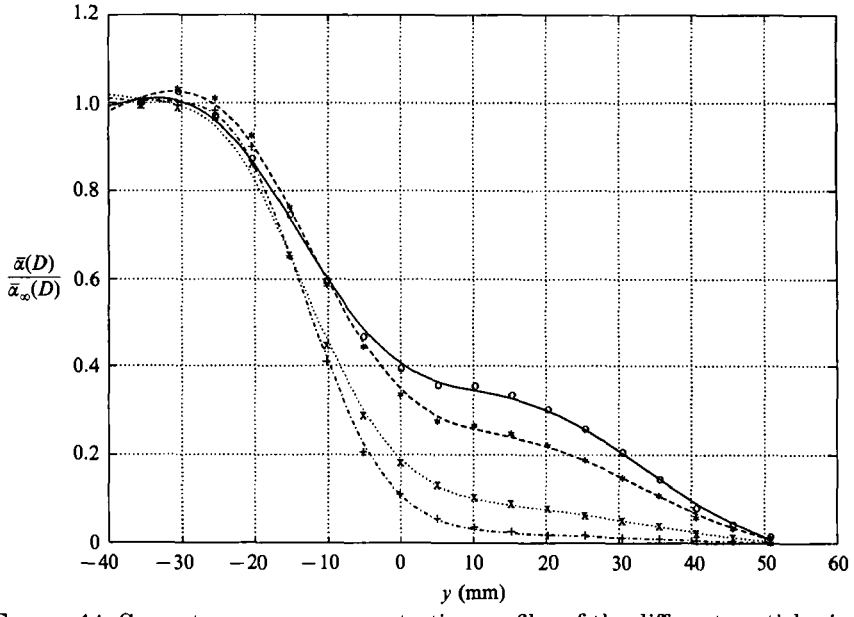

FIGURE 14. Cross-stream mean concentration profiles of the different particle size families, $x = 20.3$ cm: ○, $\bar{D} = 16.5$ μm; *, 27.0 μm; ×, 44.6 μm; +, 74.5 μm.

(*a*) the unequal decay laws existing in the inner dispersion layer;

(*b*) the presence of the plateau regions in the dispersion layer, clearly identifiable for the small droplets and hardly discernible for the large ones.

In addition, the large droplets display a very slow decay rate in the external mixing layer. This effect ultimately generates the changes in the p.d.f. function observed in the outer edge of the dispersion region, where a local recovery of the p.d.f. percentage for the large-diameter groups is seen to occur.

The increase of the 0.1–0.9 level thickness for different particle-size groups with the downstream distance is given in figure 15. The high growth rates resulting at the end of the induction region are clearly observable for the smallest size groups shown, $\bar{D} = 21$ and 35 μm. Also, an inflexion point can be identified in the mid-values of the downstream locations shown, thus supporting the previously suggested presence of curvature changes in the asymptotic, large downstream locations. The large growth rates present at the end of the induction region result in the particle concentration thickness surpassing the values measured for the longitudinal gas velocity profiles (figure 9). Since the very small particles will disperse as passive scalars, there will exist, at every downstream distance, a particle size for which the lateral dispersion will be maximum. The existence of this intermediate, enhanced dispersion size range contrasts with the experimental evidence presented in the investigation of the naturally developing flow, where no preferential particle scale was obtained in terms of the dispersion properties. This behaviour hints at the importance that the lifetimes of the large-scale vortices have in the particle dispersion evolution. Notice that, in terms of eddy lifetimes and coexistence, the forced and naturally evolving turbulent mixing layers differ significantly. In this aspect, the mixing layer evolving from a laminar boundary layer can be placed between the two cases above mentioned.

Indications of the existence of an intermediate size range for which the lateral dispersion is maximized have also been found in shear flows originating from laminar boundary layers. Numerical simulations in axisymmetric jets (Chung & Troutt 1988)

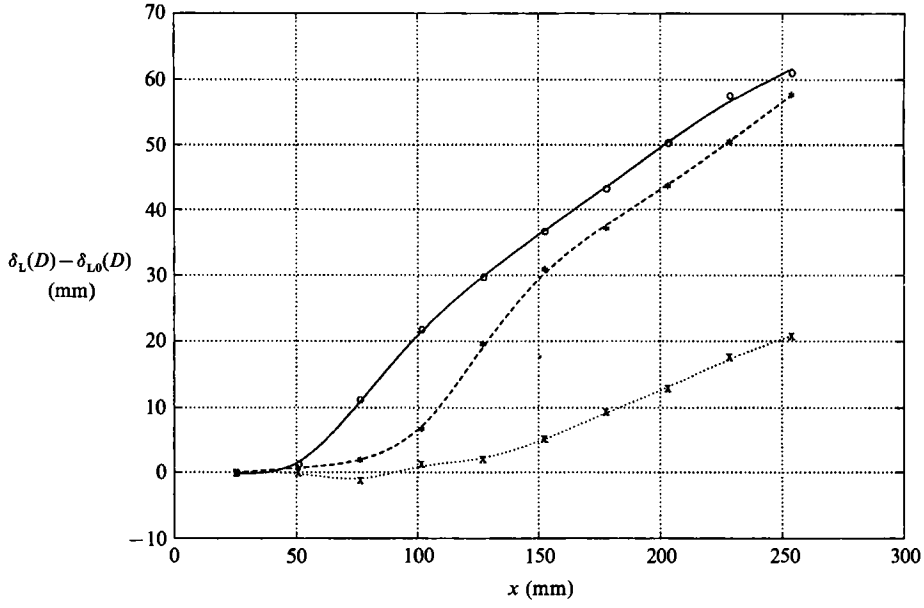

FIGURE 15. Particle size group concentration 0.1–0.9 level thickness evolution. ○, $\bar{D} = 21.1$ μm; *, 34.8 μm; ×, 44.6 μm.

and shear layers (Chein & Chung 1988) have shown that a certain range of particle sizes can achieve dispersion rates higher than those of passive markers. This particle range was characterized by having a response time of the order of magnitude of the characteristic flow time. The particles drag-to-inertia ratios were such that they were able to respond to the cross-stream velocity fluctuations existing in the shear layer and, once inside the mixing region, their inertia allowed them to reach large values of lateral dispersion.

In our study of the natural flow evolution (Part 1), we demonstrated that the non-dimensionalization necessary to obtain particle-size-independent dispersion characteristics involved the lengthscale

$$L_D = \frac{\rho_p}{\rho_g} \frac{\bar{u}_{g\infty} D^2}{18\nu}.$$

In addition, we showed that a necessary condition for the universality to exist is the dependence of the mean gas momentum upon the similarity variable y/x. Noticing the nonlinear variation of the gas momentum thickness with the downstream distance, figure 2(*b*), it can then be concluded that no size-universal dispersion curve exists in the excited mixing-layer case. Notice also that the high-particle-concentration spreading rate and gas velocity fluctuation levels that occur in the excited mixing layer lead to more severe slip velocities between the gas and the particle motion. As a result, the range of particle sizes for which the scale L_D is the controlling dispersion parameter is reduced. Physically, the lack of universality that characterizes the forced dispersion layer can be explained by the appearance of a new scale, $\Gamma/\bar{u}_{g\infty}$ (with Γ being the circulation associated with the coherent large-scale spanwise vortices), competing with the size-dispersion lengthscale in the non-dimensionalization process.

To gain further insight into this aspect, assume that, outside of the spanwise

vortices' cores, the gas velocity field can be approximated by a row of point vortices with circulation $\Gamma = \bar{u}_{g\infty}^2/2f$ (with f being the frequency of the excitation), travelling at a convection velocity $\bar{u}_c = \frac{1}{2}\bar{u}_{g\infty}$. Suppose also that in the neighbourhood of a particular vortex, the velocity field created by its own induction is the dominant effect in the dispersion process. The Eulerian equation governing the motion of small enough particles outside of the vortices' core and in a coordinate frame travelling at the vortices' convection velocity is then given by

$$\frac{\partial \boldsymbol{u}_p}{\partial t} + \boldsymbol{u}_p \cdot \nabla \boldsymbol{u}_p = \frac{\bar{u}_{g\infty}}{L_D}\frac{\Gamma}{2\pi r}\boldsymbol{e}_\theta - \frac{\bar{u}_{g\infty}}{L_D}\boldsymbol{u}_p \; \forall r > r_c, \tag{1}$$

where $2r_c$ represents the dimension of the vortex viscous core.

With characteristic scales being represented by L, T and U, the terms appearing in (1) are respectively proportional to

$$U/T; \quad U^2/L; \quad (\bar{u}_{g\infty}\Gamma)/(L_D L); \quad \bar{u}_{g\infty}/L_D U,$$

which implies

$$T = L_D/\bar{u}_{g\infty}; \quad U = (\bar{u}_\infty \Gamma/L_D)^{\frac{1}{2}}; \quad L = (\Gamma L_D/\bar{u}_{g\infty})^{\frac{1}{2}}. \tag{2}$$

Therefore, in a coordinate system travelling with the vortex, the time is proportional to the scale L_D. On the other hand, there is a linear relationship between the Eulerian downstream coordinate and the Lagrangian average vortex evolution time. As a result, an alternative non-dimensionalization, tailored to account for the effect of the dominant gas velocity flow scale, could be to scale the cross-stream coordinate with $(\Gamma L_D/\bar{u}_{g\infty})^{\frac{1}{2}}$ and the downstream location with L_D.

Notice that the mean dispersion field measured at a given point (x, y) in the laboratory frame of reference corresponds to an averaging process that includes longitudinal distances from the vortices' core between $-\frac{1}{2}\lambda$ and $\frac{1}{2}\lambda$, and eddy evolution times ranging between $(2x-\lambda)/\bar{u}_{g\infty}$ and $(2x+\lambda)/\bar{u}_{g\infty}$ in the frame travelling with the vortices. Observe then, that if x is non-dimensionalized with L_D, the non-dimensional times over which the average is carried out are $(2x-\lambda)/L_D$ and $(2x+\lambda)/L_D$. Expanding the evolution of a generic non-dimensional field quantity g around the central non-dimensional time $2x/L_D$ gives

$$g(2x/L_D+\tau) = g(2x/L_D) + \mathrm{d}g/\mathrm{d}t|_{t-2x/L_D}\tau + \tfrac{1}{2}\mathrm{d}^2g/\mathrm{d}t^2|_{t-2x/L_D}\tau^2 + o(\tau^2). \tag{3}$$

Averaging now for $\tau \in [-\lambda/L_D, \lambda/L_D]$:

$$\bar{g}(2x/L_D) = g(2x/L_D) + \tfrac{1}{6}\mathrm{d}^2g/\mathrm{d}t^2|_{t-2x/L_D}(\lambda/L_D)^2 + o(\lambda/L_D)^4. \tag{4}$$

Expression (4) reveals that to obtain collapse with the non-dimensionalization

$$x/L_D, \quad y/(\Gamma L_D/\bar{u}_{g\infty})^{\frac{1}{2}}, \tag{5}$$

it must be

$$1/g\,\mathrm{d}^2g/\mathrm{d}x^2\lambda^2 \ll 1. \tag{6}$$

Since the cross-stream dispersion lengthscale increases with the particle diameter, the above analysis is specially relevant for the smallest particle sizes when not one but an infinite row of vortices causes the dispersion of the droplets. For large droplets, however, the dispersion lengthscale is such that, eventually, the closest vortices will also have a substantial effect on the dispersion properties. Also, there is an upper particle size limit for which the lengthscale L_D remains meaningful. The non-dimensionalization proposed in (5) should, therefore, works best for the smallest particle sizes. In addition and, according to the inequality (6), the universality will hold as far as the function g does not have regions with changes characterized by a

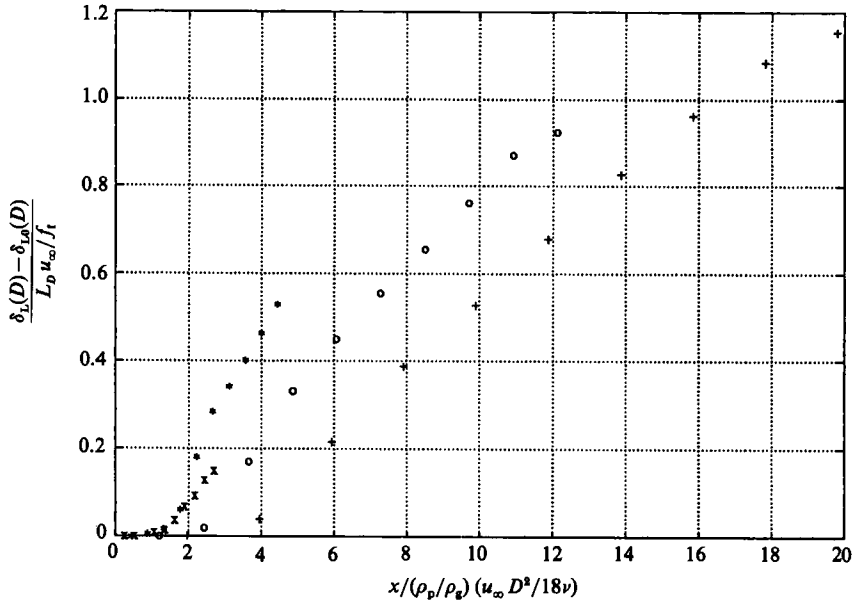

FIGURE 16. Particle size group 0.1–0.9 level thickness evolution non-dimensionalized with the variables proposed in expressions (5). ×, $\bar{D}$ = 16.5 μm; ○, 21.1 μm; *, 34.8 μm; ×, 44.6 μm.

radius of curvature of the order of λ, with complete collapse being obtained when g is a linear function. In particular, the high curvature present in the induction region for the level thickness evolution inhibits the success of the non-dimensionalization (5) for this function. This behaviour is confirmed in figure 16. The failure of the non-dimensionalization can be tracked down to the induction region. Also, the parallel trends displayed by the two smaller diameter groups in the furthest x-locations hint at the satisfactory behaviour of the procedure in reduced curvature regions and small particle sizes.

If the small-particle size dispersion is characterized by functions possessing small enough curvature for expressions (5) to non-dimensionalize them properly, it means that the transversal positions occupied by the particles scale as

$$\delta_D \propto \frac{\bar{u}_{g\infty} D}{(18\rho_g/\rho_p \nu f)^{\frac{1}{2}}} \tag{7}$$

and, therefore, are proportional to the size diameter involved. In addition, notice that the effect of the forcing frequency is to decrease the transversal lengthscale proportionally to $f^{-\frac{1}{2}}$. This strong dependence of the spreading rates on the forcing frequency of the mixing layer is consistent with the mean flow visualizations shown previously, where the decrease of the forcing frequency from f_f = 140 to 72 Hz resulted in a substantial decrease of the spreading rate of the dispersion layer (figures 6*a* and 6*b*).

6. Temporal organization of the particle dispersion field

From the instantaneous flow visualization presented in figures 17(*a*) (f_f = 140 Hz) and 17(*b*) (f_f = 72 Hz) one can conclude that the forced mixing layer possesses a high degree of inhomogeneity and coherency in the particle concentration field. The

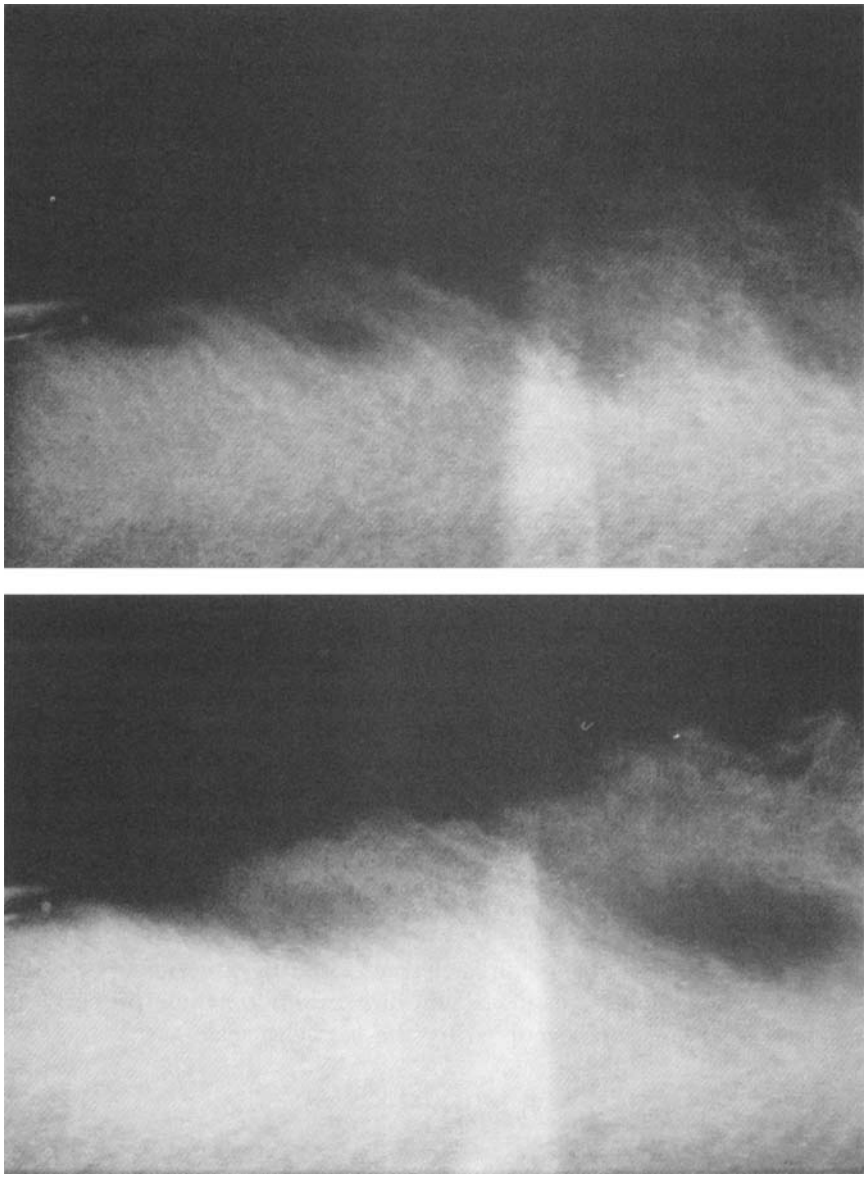

FIGURE 17. (a) Instantaneous flow visualizations of the 90° particle light scattering. Mixing layer forced with $f_f = 140$ Hz. (b) Instantaneous flow visualization of the 90° particle light scattering. Mixing-layer forced with (a) $f_f = 140$ Hz and (b) $f_f = 72$ Hz.

dispersion region is seen to be dominated by tongue-shaped streaks emanating periodically from the core of the spray, and engulfing extensive areas in which the particle concentration appears to have extremely low values. Notice that the point of emergence of the dispersion structures shifts to more negative cross-stream positions as one moves downstream.

The high growth rates governing the first steps of the dispersion process are especially visible in figure 17(a), where one can observe a remarkable difference between the size of the structure forming next to the splitter plate and the one

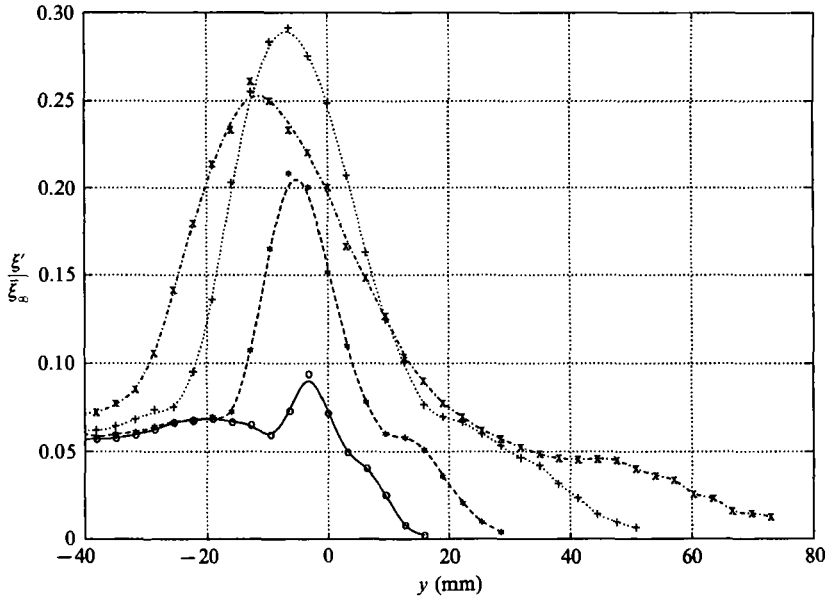

FIGURE 18. Cross-stream fluctuating laser attenuation r.m.s. profiles: ○, $x = 5.1$ cm; *, 10.2 cm; +, 17.8 cm; ×, 25.4 cm.

immediately downstream of it. Also clearly appreciable is the growth of the polar angle swept by the streaks for increasing downstream locations. This evolution eventually results in their leading edge touching the root region of the upstream structure, reaching a state in which the dispersion region is composed of a row of connecting streaks leaving in their centres a depletion area. The shape and extension of the large dispersion structures is a manifestation of their connection to the large-scale vortices dominating the underlying turbulent gas motion. The flow visualizations shown in figures 17(*a*) and 17(*b*) bear a striking resemblance to the classical pictures of the large-scale eddies known to be present in high-Reynolds-number mixing layers (Brown & Roshko 1974). Furthermore, these flow visualizations revealing the presence of an organized dispersion structure are similar to those reported previously by Crowe, Chung & Troutt (1988) and Lázaro & Lasheras (1989). Superimposed on the large-scale organization are irregularities and small-scale variations in the concentration field which can also be identified in the visualizations. At the farthest downstream locations shown, however, the isotropic structure appears just as a small modulating effect over the large dispersion streaks and its smearing action seems not to break the spatial coherency displayed by the organized motion. Notice also that for the mixing layer forced with its initial most unstable frequency, figure 17(*a*), the late stages of flow development exhibits a very small growth of the dispersion cross-stream scale.

Analogously to the analysis of the naturally developing flow (Antonia 1983), the attenuation signal can also be used to gain further insight into the particle concentration field in the forced flow case.

The downstream evolution of the attenuation r.m.s. profiles for the mixing layer being forced at the subharmonic frequency, $f_t = 72$ Hz, is shown in figure 18. The high levels of particle dispersion activity that characterize the forced mixing layer can be immediately noticed. At $x = 25.4$ cm the peak r.m.s. attenuation in the excited flow is more than twice the value found in the natural mixing layer.

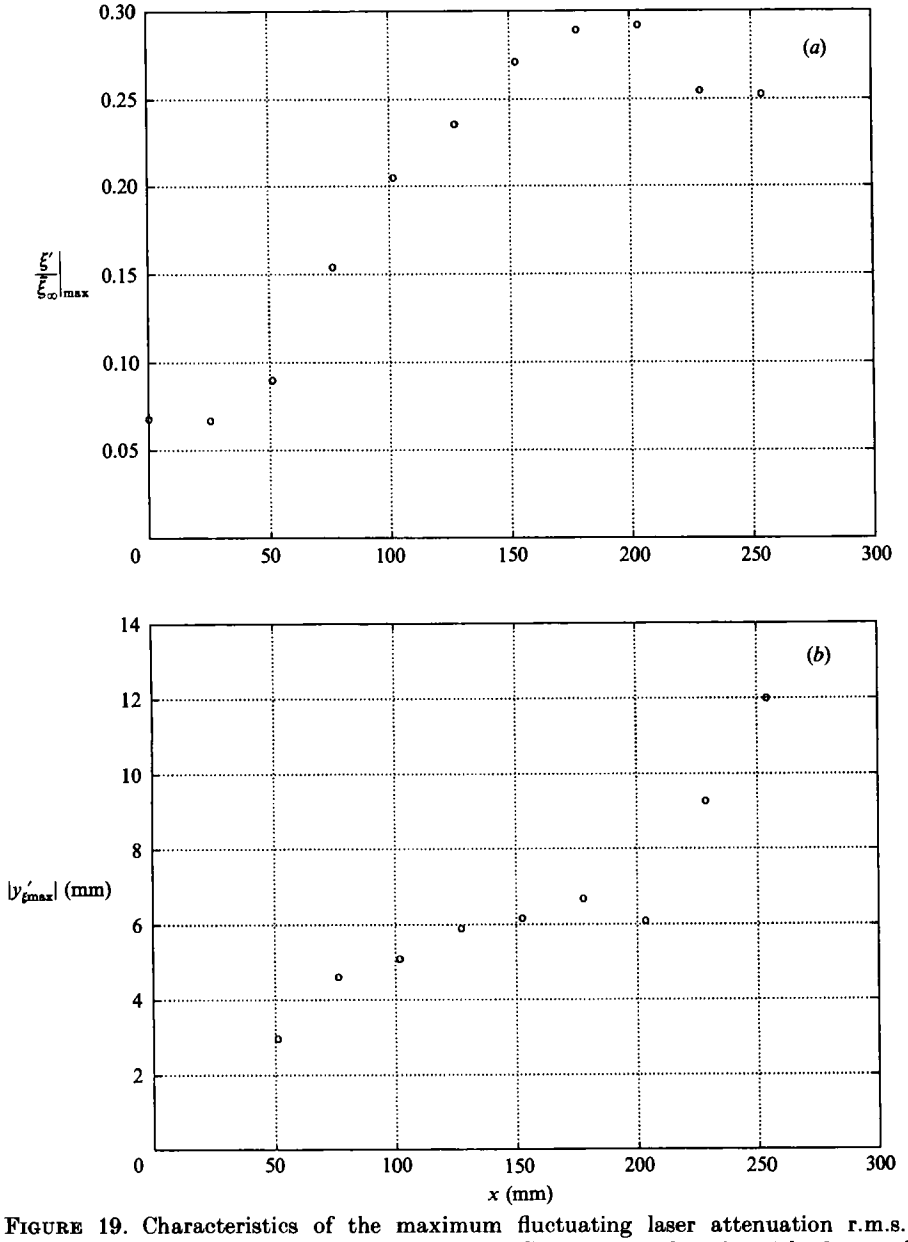

FIGURE 19. Characteristics of the maximum fluctuating laser attenuation r.m.s. value. (*a*) Downstream evolution of the maximum. (*b*) Cross-stream location (absolute value) of the maximum.

Figures 19(*a*) and 19(*b*) show the downstream evolution of the maximum r.m.s. attenuation and its cross-stream localization (expressed by its absolute value) respectively. Notice that the r.m.s. evolution is characterized by the following characteristics: (*a*) the peak in the r.m.s. profile is seen to grow up to $x = 17.8$ cm. The last location shown exhibits, however, an important decrease in this value; (*b*) the location of the r.m.s. peak value appears to have a sudden shift towards the free-stream side of the spray at $x = 25.4$ cm. In addition, the region of enhanced r.m.s. level has become much wider for this downstream location.

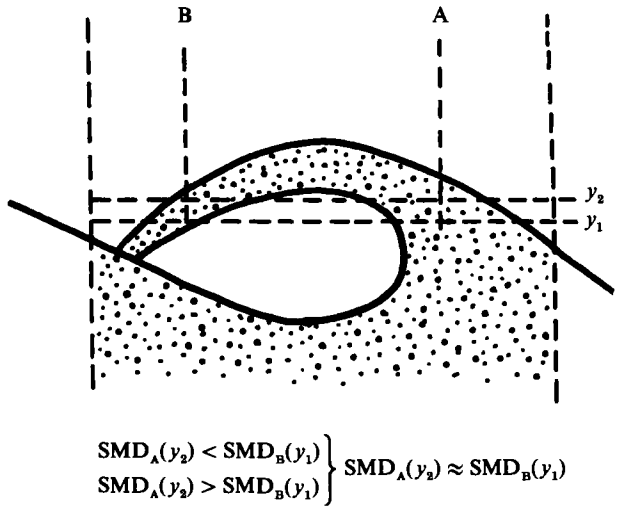

FIGURE 20. Large dispersion streak measurement volumes in the central dispersion region when sampling at a given cross-stream position.

The connection of consecutive streaks appears to be the event responsible for the existence of these phenomena. Before the connection is completed, the emergence point of the streaks is the region where higher r.m.s. values are expected. The exact location of the maximum r.m.s. depends on the attenuation decay law and on the width of the root of the streaks. In addition, the peak in the attenuation r.m.s. is very sharp, suggesting the small jitter existing in the emergence point of consecutive streaks. However, once the inter-streak connection is completed, the r.m.s. around the streak emergence point must decrease, because the duty cycle of the attenuation spikes associated with the passage of regions of high particle concentration is closer to one. The r.m.s. peak now shifts to regions where the spikes are more intense, i.e. the central depletion region. The r.m.s. activity in all the cross-stream locations touching the depletion area must be, in fact, of the same order of magnitude. As a result, a broadening of the region of enhanced r.m.s. values occurs.

Notice that the streak connection may also be responsible for the p.d.f. homogenization patterns described in the previous section. Considering a given cross-stream coordinate, a definite change in the p.d.f. behaviour will occur only if an ascending streak is present or if both an ascending and a descending streak region touch the specific measurement volume. If the streaks are associated with a negative gradient of the mean particle size along their polar angle (i.e. there is a continuous increase in the small particulate p.d.f. as we move along the curvature of the streak), a region of frozen p.d.f. can be expected to occur in the mid-portions of the dispersion layer. To illustrate this point, assume the above-described mean diameter gradient and compare the p.d.f. measured at two cross-stream locations, y_1 and y_2 ($y_2 > y_1$, figure 20), which are wet by both ascending and descending streak regions. The decrease in the mean diameter that occurs in the ascending branch of the streak when measuring at y_2 is compensated for by the diameter increase associated with the descending streak. The change in the p.d.f. homogenization pattern described in the previous section was found to occur around $x = 15$ cm, somewhat upstream of the dislocation found in the r.m.s. pattern, located at $x = 20$ cm. This difference in the downstream coordinates for the appearance of the two phenomena was to be

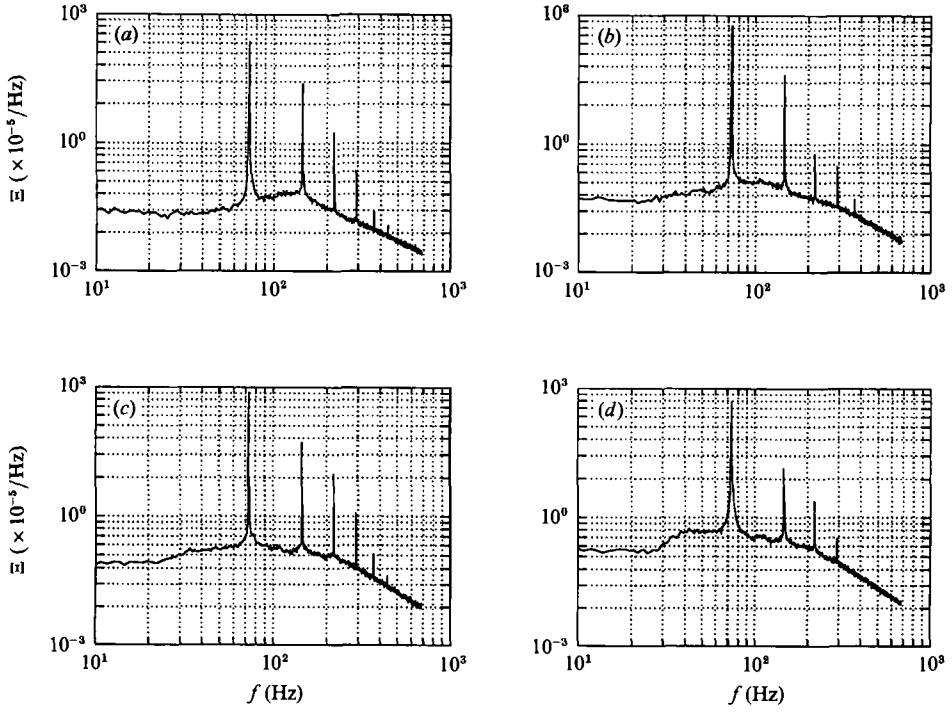

FIGURE 21. Downstream evolution of the laser attenuation power spectrum, $y = 0$. (*a*) $x = 7.6$ cm, (*b*) $x = 12.7$ cm, (*c*) $x = 17.8$ cm, (*d*) $x = 25.4$ cm.

expected, since the change in the r.m.s. pattern occurs only when the streaks are connected, and the p.d.f. homogenization requires the existence of the two streak branches.

The external region of the dispersion layer is also characterized by the stabilization of the r.m.s. profile and subsequent formation of an inflexion point (figure 18). As was the case with the natural flow, this area is created by the alignment of the external portion of the dispersion structure along the stream-wise direction. However, the stabilization effect never seems to be powerful enough to create a second peak in the cross-stream attenuation r.m.s. profile. This behaviour contrasts with the measurements of passive scalar dispersion performed in turbulent plane mixing layers under similar experimental conditions (Wynanski, Oster & Fiedler 1979). Although the triple inflexion profile of the mean concentration is found in the passive scalar experiments, their r.m.s. fluctuations are characterized by two distinct, symmetric peaks at the edges of the mixing layer, separated by an area of smaller activity. The picture that can be extracted from the passive scalar measurements is, therefore, the existence of a central dispersion region, with high mixing levels, and two external layers where the intermittency of the scalars produces localized peaks. In the present dispersion case, however, the core of the vortices appear practically depleted of particles, and the dispersion structures are characterized by sharp contours.

The downstream evolution of the spectral content of the attenuation signal is presented in figure 21. The mixing-layer excitation creates spectral levels 40 dB above the ones found in the natural flow. Hints of progressive smearing in the coherent signal appear at the downstream end of the present measurement window ($x = 25.4$ cm). Notice that, for this position, the ratio of the coherent peak to the spectral baseline level becomes smaller. Observe also the increase in the low-

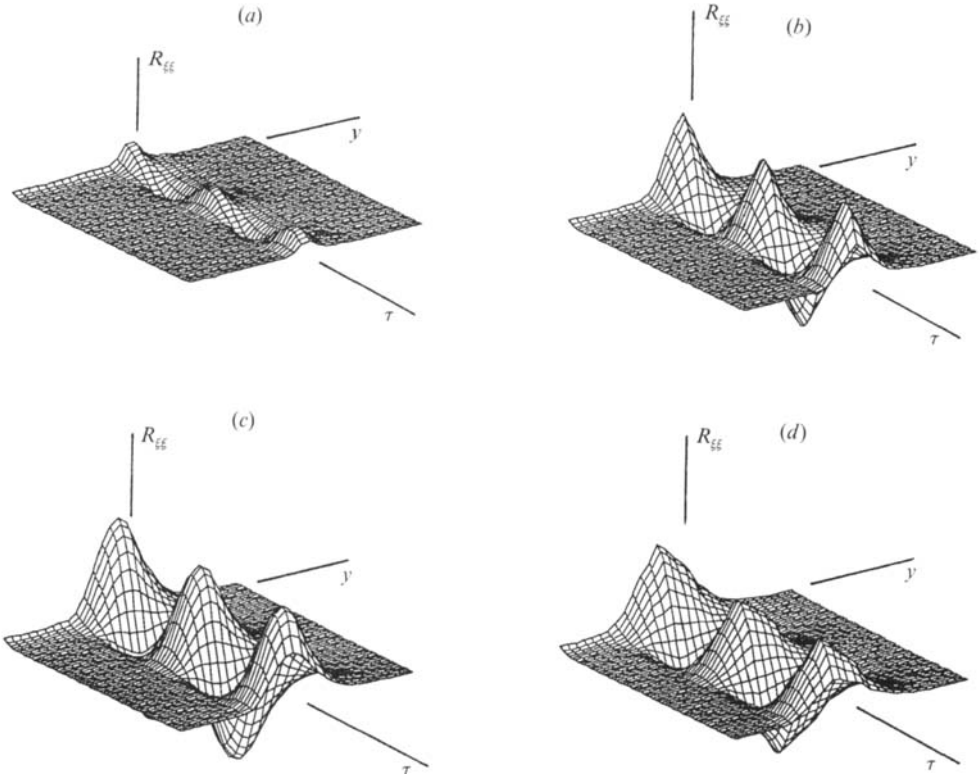

FIGURE 22. Laser attenuation temporal autocorrelation variation along the cross-stream coordinate. Each surface corresponds to a given downstream distance. (*a*) $x = 7.6$ cm (*b*) 15.2 cm, (*c*) 20.3 cm, (*d*) 25.4 cm.

frequency spectral content identifiable at this downstream location. The much cleaner spectral response obtained in the attenuation measurements when compared with those of the velocity (figure 5) is worth mentioning. The difference in the nature of the gas velocity and particle attenuation measurements and the enhanced particle response to low-frequency fluctuations are responsible for this distinct behaviour.

The strong periodicity of the attenuation signal is equally visible in the temporal autocorrelation cross-stream surfaces shown in figures 22 and 23. The cross-stream asymmetry of the contour plots is apparent from a downstream distance of $x = 15.2$ cm on, contrasting with the symmetrical shape exhibited by the surface at $x = 7.6$ cm. This observation is consistent with the asymmetry being generated by the streamwise alignment of the streaks, since it takes some downstream distance before the streak alignment occurs.

The cross-stream variation of the transport average $\overline{u_g \xi}$ is shown in figure 24, for a downstream distance $x = 10.2$ cm. The mixing region is characterized by negative values of the transport average, with peak values two orders of magnitude higher than those encountered in the naturally developing flow. The region of intense activity is located around the cross-stream location where the r.m.s. of the attenuation signal shows its peak value, and therefore close to the streak emergence point. The strong negative values encountered confirm the spatial shift between the core of the vortices (where positive fluctuating longitudinal velocities are to be expected) and the location of the streak emergence. In order to obtain positive cross-correlation values, a certain temporal shift must be introduced in the signal. This

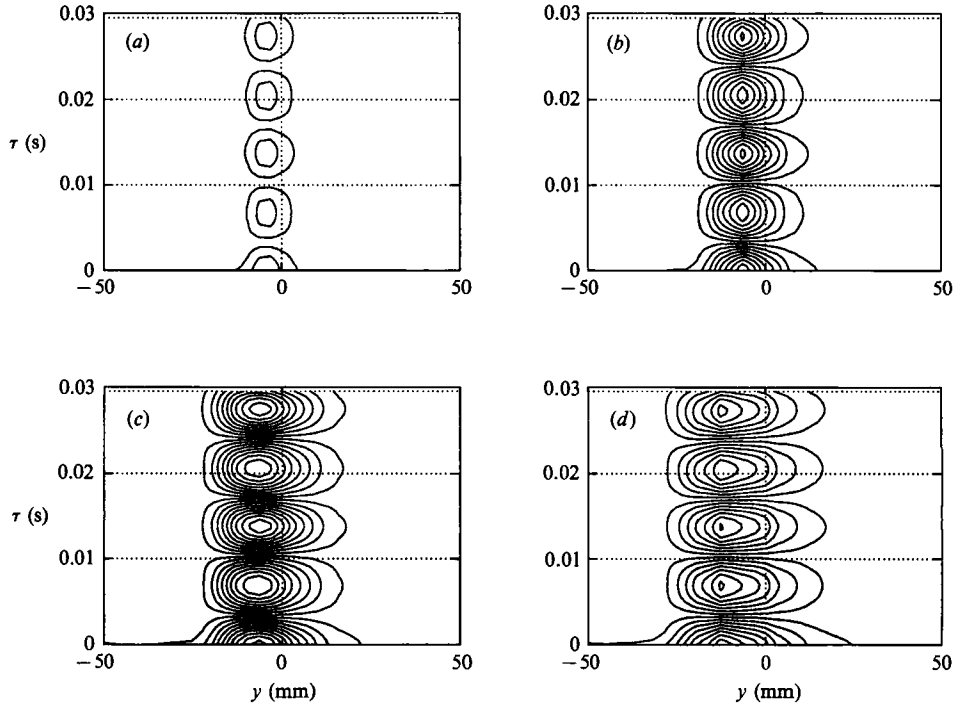

FIGURE 23. Laser attenuation temporal autocorrelation variation along the cross-stream coordinate. Isocontour plots of surfaces displayed in figure 22 (*a*) $x = 7.6$ cm, (*b*) 15.2 cm, (*c*) 20.3 cm, (*d*) 25.4 cm.

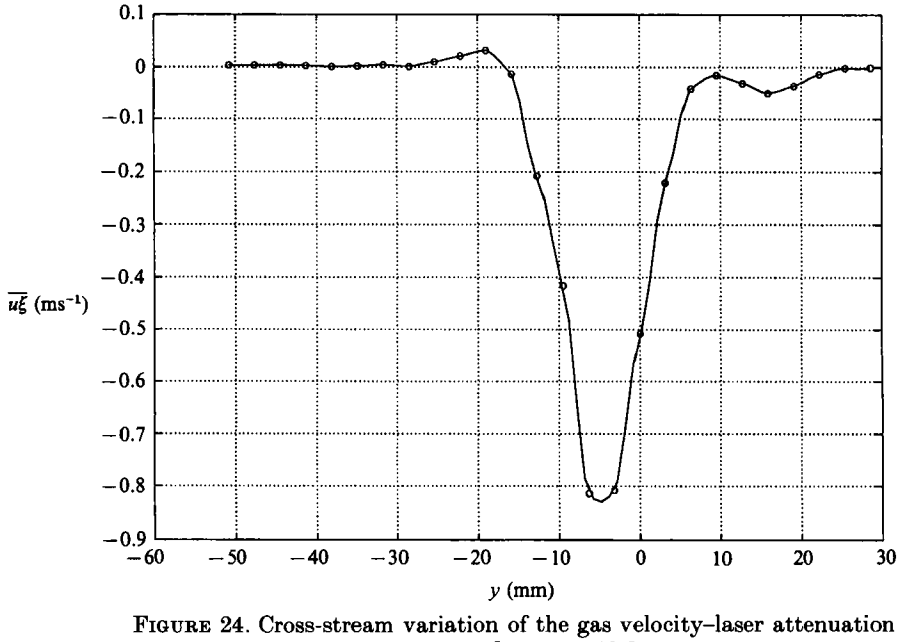

FIGURE 24. Cross-stream variation of the gas velocity–laser attenuation transport product, $x = 10.2$ cm.

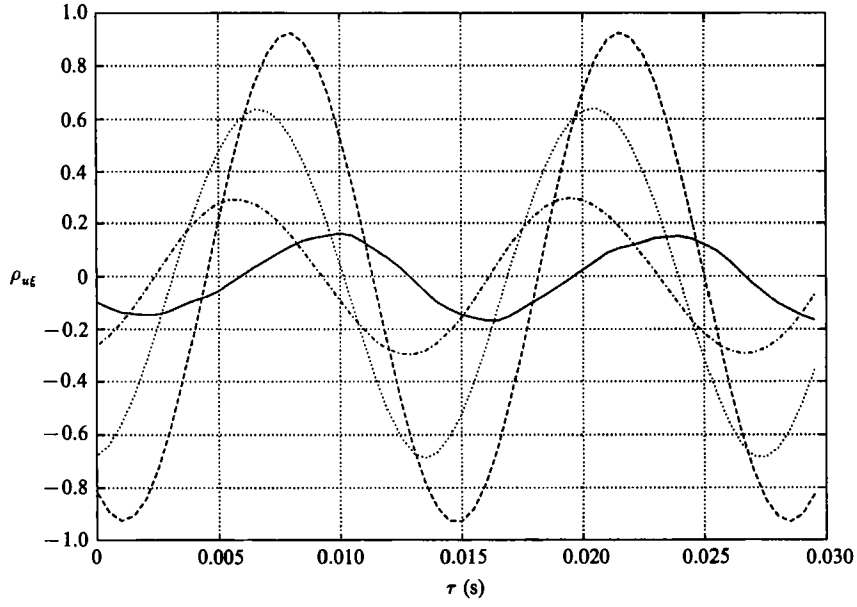

FIGURE 25. Gas velocity–laser attenuation temporal cross-correlation coefficient, $y = -3.1$ mm: ——, $x = 5.1$ cm; – – –, 10.2 cm; ....., 15.2 cm; —·—·—, 20.3 cm.

aspect can be observed by analysing the temporal cross-correlation coefficient, $\rho_{u\xi}(\tau)$. Plots of this variable are given in figure 25. Observe the high values attained by the cross-correlation coefficient, indicating the strong correlation between the velocity and attenuation fields. Notice that at $x = 10.2$ cm the correlation is almost perfect. Observe also the temporal shift necessary to reach the maximum positive cross-correlation value. This maximum is achieved at about $\tau \approx 7.5 \times 10^{-3}$ s, which gives, for an excitation period of $T_l = 13.8 \times 10^{-3}$ s a separation distance close to $\frac{1}{2}\lambda$. Therefore these measurements indicate that the streaks emerge in the braid region connecting consecutive vortices. Notice, as one moves downstream, the consistent decrease in the delay time for which the maximum cross-correlation is achieved. It is found that the whole cross-stream region displaying high cross-correlation levels is characterized, at a given x, by similar time-delay values. Thus, the shift appears in a consistent way throughout the mixing region. In addition, observe that the effect of the shift is to reduce the time delay at which the maximum correlation occurs. Since what is computed is the average $\overline{u(t)\,\xi(t+\tau)}$, this means that the positive values of the fluctuating attenuation (streak emergence regions) are being displaced towards the core of the vortex structure adjacent to the one from which they originated. The amount of the displacement is approximately constant for equally spaced downstream locations. Two possible mechanisms can account for this effect: (*a*) the existence of a relative longitudinal velocity between the vortical structures and the streaks, and (*b*) the incorporation in the streaks of particles whose emergence point is located farther away from the core of the vortices from which they originate.

At this point, it is not possible to elucidate the relative weight that each of the two effects may have towards the observed shift. Measurements of the amount of the shift indicate that a relative velocity of 1.6 ms^{-1} in the streak emergence region will

be necessary to account for the observed data if only the first effect is assumed to be responsible for it.

7. Phase-average measurements

The high degree of organization and coherency exhibited by the particle concentration field in the forced mixing layer makes it an ideal choice for performing excitation phase-conditioned measurements. The small degree of jitter that characterizes the particle dispersion in the forced flow is demonstrated by the 90° light scattering stroboscopic flow visualization of the particle dispersion field in the subharmonically ($f = 72$ Hz) excited mixing layer (figure 26). The picture was obtained by superimposing ten consecutive flash pulses in phase with the forcing function. Although the multiple exposure smooths out the small-scale inhomogeneities observed in the instantaneous visualizations, it preserves the characteristics of the large-scale dispersion.

The phase-average measurements of the attenuation field are given in figures 27 and 28(i) and 28(ii) (Plate 1). These measurements were obtained averaging over more than 500 structures and provide a detailed record of the streak formation process discussed above. Every surface corresponds to a given downstream location. The phase coordinate, ϕ, represents the time delay of the measurement with respect to some arbitrary origin in the forcing function waveform. This time delay has been referred to the period of the excitation and converted to an angular variable. In order to have the emergence point of the streaks always at the same phase location, a phase shift has been performed at every downstream position. The shift is travelling at almost the convection velocity of the underlying vortices. As a result, the dispersion structures seem to be stationary with respect to the observer. Notice that at $x = 10.2$ cm the streak is already clearly observable. At a downstream distance of $x = 20.3$ cm the interstreak connection process has already been achieved, sharply defining the formation of a central depletion region. Observe also the accumulation of droplets that is taking place at the edge of the depletion region facing the core of the spray. This local effect can be noticed in the constant-phase cuts of figure 29. Notice how, at the inner edge of the depletion area, there is an accumulation of particles. The location of the inner accumulation region moves towards the undisturbed region with increasing x.

The data shown in figure 28 offer quantitative information that can be used to describe the evolution of the streaks. The particle transport can be described by the geometrical evolution of the streak's centrelines and by the decay law that the attenuation exhibits along them.

Rigorously, the definition of the streak centreline can be given as the curve in the phase (ϕ, y) plane satisfying:

$$\left(\frac{\lambda}{2\pi}\right)^2 \frac{\mathrm{d}\phi}{\xi_\phi} = \frac{\mathrm{d}y}{\xi_y} = \frac{\mathrm{d}s}{|\nabla\xi|}, \tag{8}$$

i.e. the curve whose tangent is parallel to the gradient of ξ. The definition of the centreline is completed when one of its points, say the one corresponding to an arbitrary origin of the arclength s, is given:

$$\boldsymbol{x}_s|_{s=0} = \boldsymbol{x}_{s0}. \tag{9}$$

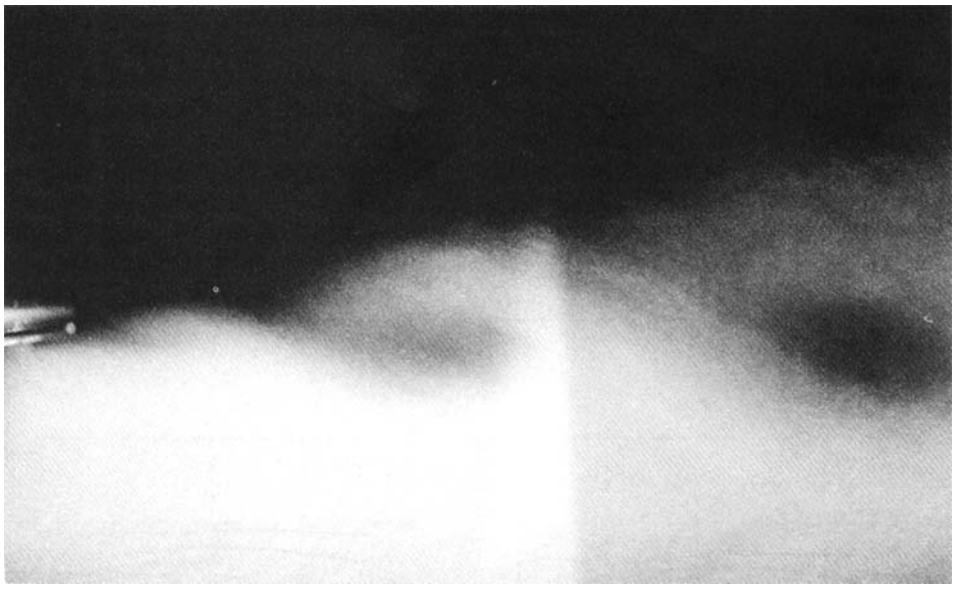

FIGURE 26. Multiple exposure flash pulse visualization of the 90° particle light scattering. Mixing layer forced at $f_f = 72$ Hz. Flash pulses are triggered by the forcing function to create a stroboscopic effect.

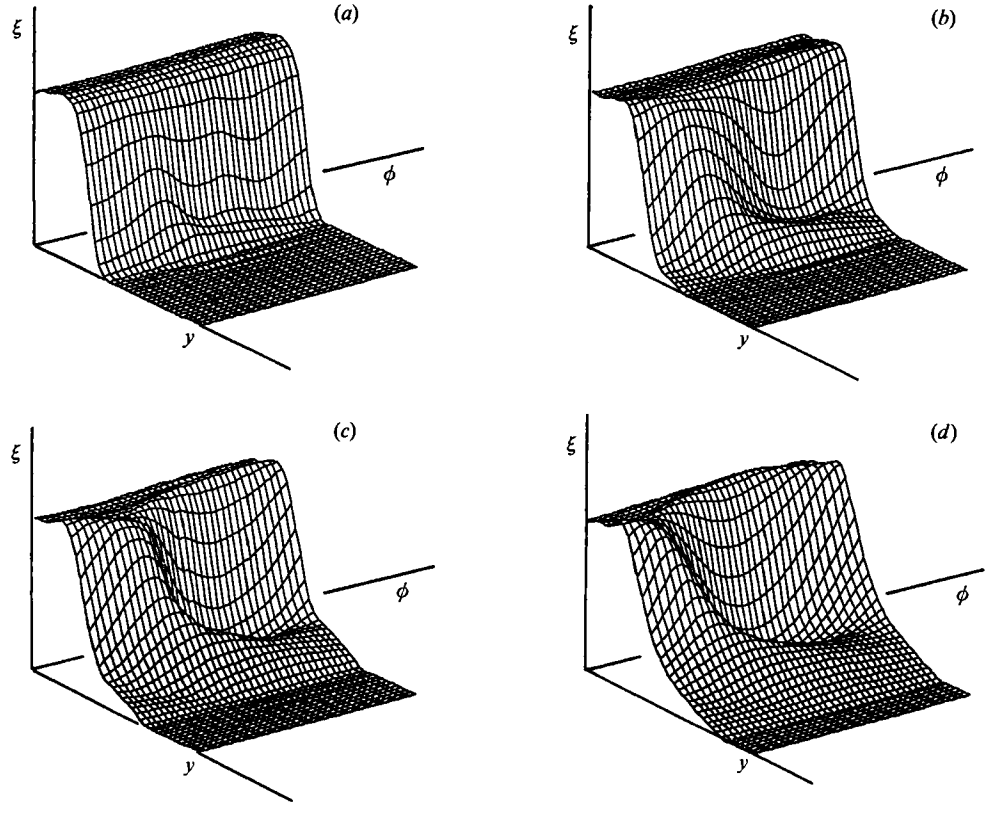

FIGURE 27. Laser attenuation phase-average surfaces. Each surface is characterized by a fixed downstream distance and represents the variation of the laser attenuation with the cross-stream coordinate and forcing function phase variable. (*a*) $x = 5.1$ cm, (*b*) 10.2 cm, (*c*) 15.2 cm, (*d*) 20.3 cm.

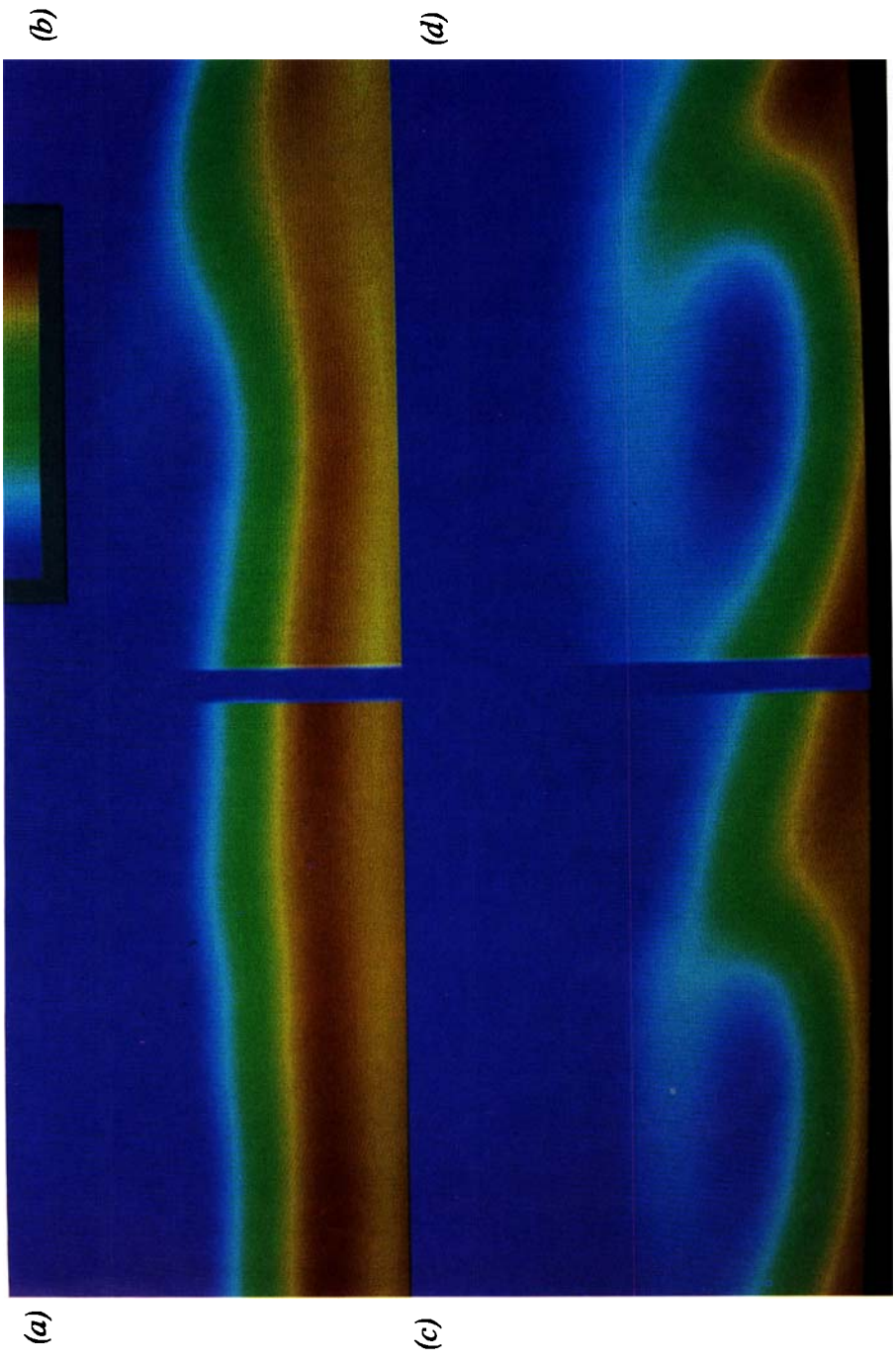

FIGURE 28(ii). Laser attenuation phase-average measurements. Pseudo-colour representation of the surfaces displayed in figure 27. Intensity scale appears in the upper right corner of the photograph. Blue denotes low attenuation and therefore corresponds to low particle concentration. Red and yellow denote intense presence of particulate. (*a*) x = 5.1 cm, (*b*) 10.2 cm, (*c*) 15.2 cm, (*d*) 20.3 cm.

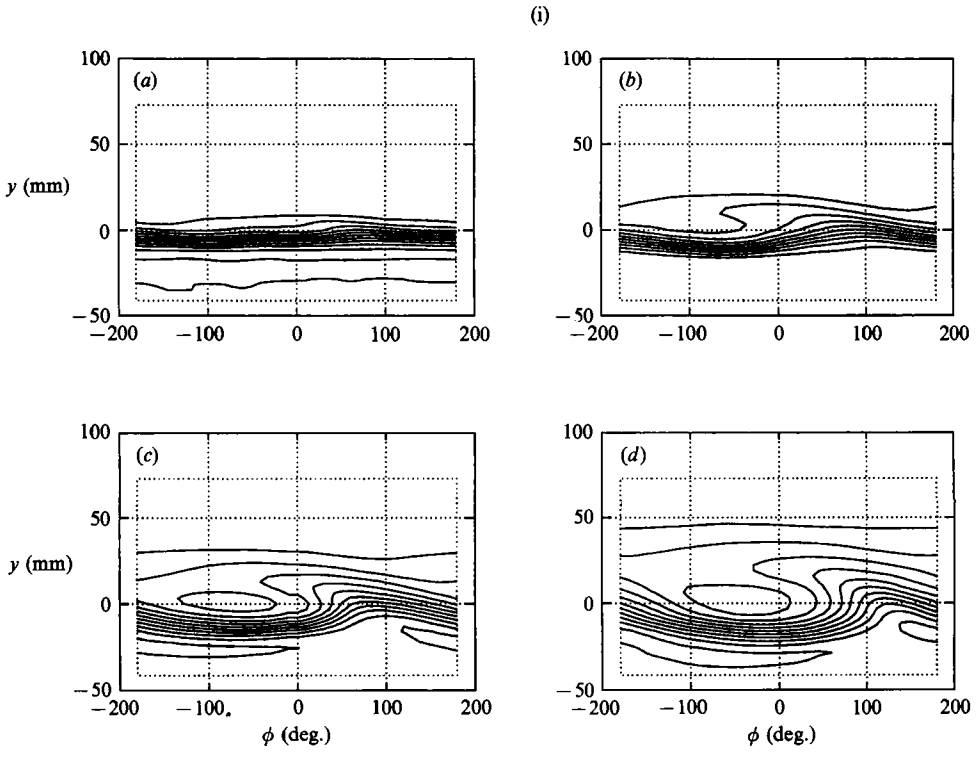

FIGURE 28. (i) Laser attenuation phase-average measurements. Isocontours plots of surfaces of figure 27. Isocontour levels located at $\xi_{\text{ph.av.}}/\xi_{\infty} = 0.05, 0.15, \ldots, 1.05$. (*a*) $x = 5.1$ cm, (*b*) 10.2 cm, (*c*) 15.2 cm, (*d*) 20.3 cm.

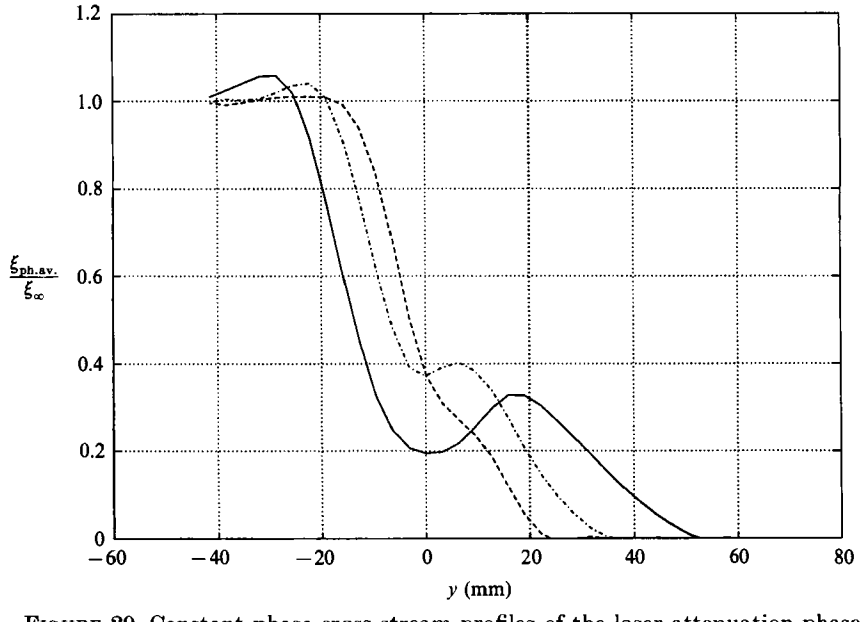

FIGURE 29. Constant-phase cross-stream profiles of the laser attenuation phase-average function, $\phi = -30°$: ——, $x = 10.2$ cm; —·—·—·, 15.2 cm; – – –, 20.3 cm.

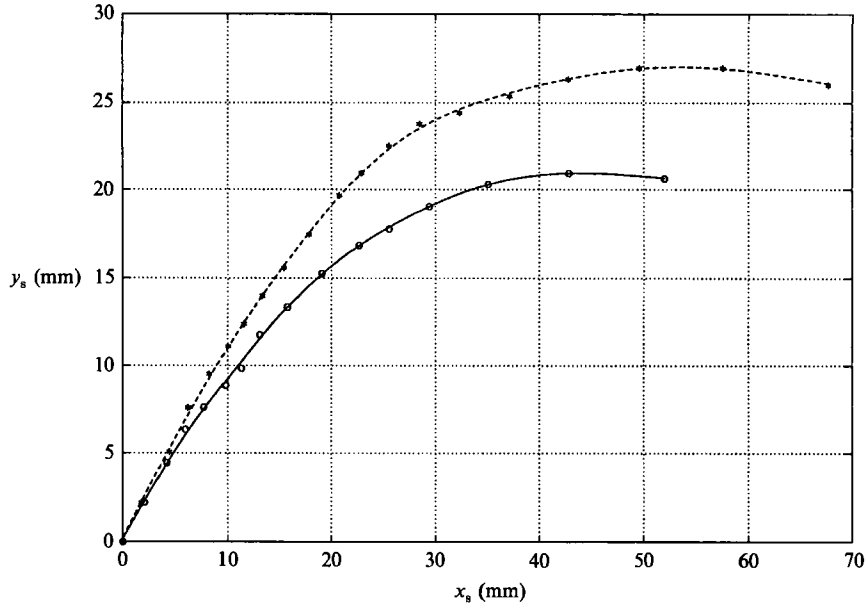

FIGURE 30. Large-scale streak centreline geometry as obtained from the data presented in figure 28. The phase variable has been converted to length units and the origin has been selected as the streak's emergence point. ○, $x = 10.2$ cm; *, 20.3 cm.

Anchoring points that can be easily located are the ones defining the tip of the streak. In this area the attenuation is slowly decaying in the phase coordinate and the streak centreline $P_s(\phi_s, y_s)$ can be defined by

$$\left.\frac{\partial \xi}{\partial y}\right|_{\phi_s} = 0. \tag{10}$$

The small values of the attenuation gradient in this region, however, preclude a numerical solution of (8) to compute the streak centreline curve. A problem arises from the instability of the numerical scheme in regions with small $|\nabla \xi|$ values (computational errors will deviate the curve solution either to the background area or to the depletion hole). To overcome this difficulty, an approximation to (8) has been performed graphically by creating high-definition contour plots similar to the ones shown in figure 28. An anchoring point in the leading-edge region of the streaks is selected. Subsequent points of the centreline are obtained by graphically determining the closest point in the adjacent isocontour. The result of this procedure is shown in figure 30. The phase coordinate has been multiplied by $\frac{1}{360}\bar{u}_{gc}/f$ to give length dimensions. In addition, both streak centreline coordinates have been referred to the location of the emergence point.

The geometry of the streak is composed of an almost straight line (in the emergence point region) that bends backwards to align itself along the streamwise x-direction. There is an increase in the radial coordinates and polar angles swept by the streak as we move downstream. In addition, the angle that the emergent streak forms with the streamwise direction is higher for $x = 20.3$ cm, possibly indicating that the ratio of the vertical to longitudinal particle velocities has increased as one moves downstream.

The attenuation along the streak centreline is shown in dimensionless form in

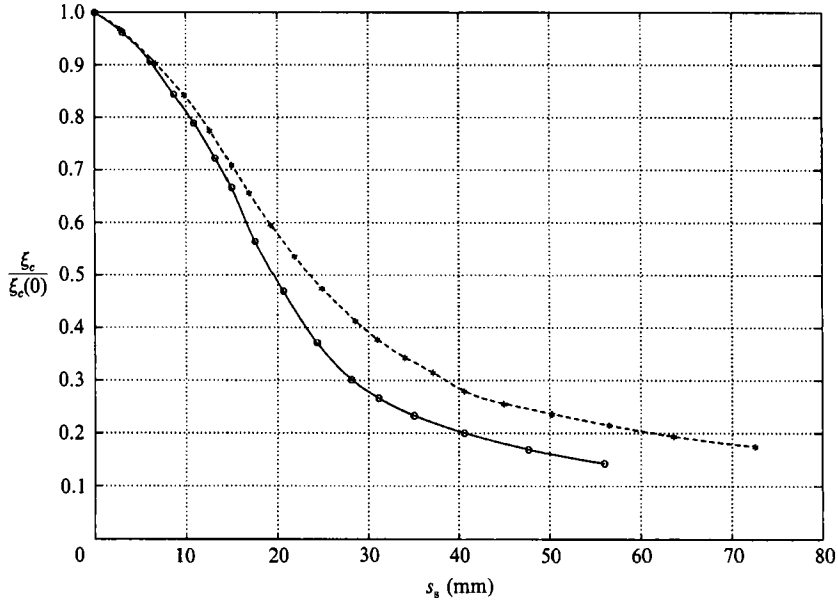

FIGURE 31. Laser attenuation decay along the streak centreline. Origin is as in figure 30. Length coordinate is the arclength along the streak. ○, $x = 10.2$ cm; *, 20.3 cm.

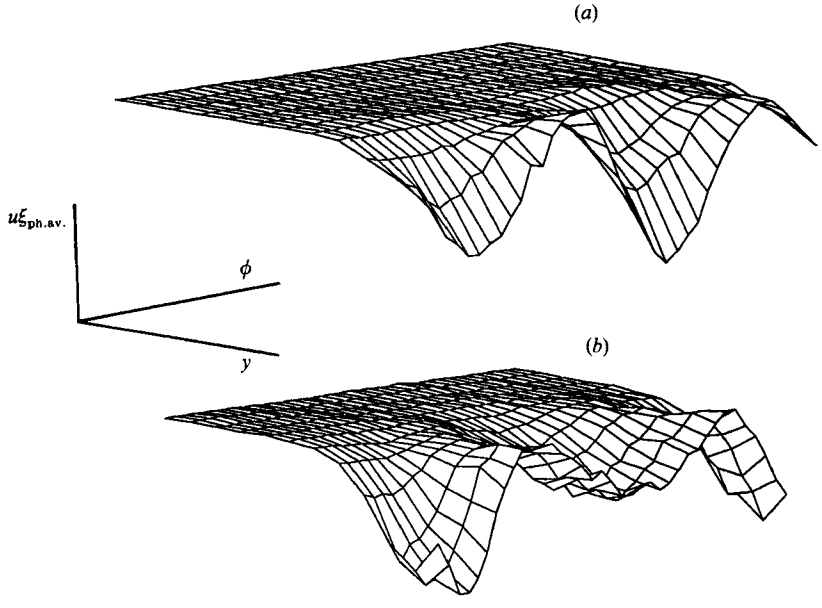

FIGURE 32. Cross-stream variation of the longitudinal gas velocity–laser attenuation phase-average product. Each surface corresponds to the downstream distance (*a*) $x = 10.2$ cm, (*b*) $x = 20.3$ cm.

figure 31. The normalizing attenuation is the one found at the emergence region and the resulting dimensionless curve has been displayed versus the arclength along the streak. The attenuation shows a very fast decrease in the regions close to the core of the spray and a relaxation in its decay when the streak aligns itself with the streamwise direction. The effects contributing to the attenuation decay along the

streak are the initial boundary-layer attenuation profile and the existence of particle velocity gradients along the streak. The relaxation of the attenuation decay observed in the external sections of the centreline suggests that this region is characterized by a constant particle velocity. This conclusion is consistent with the alignment of the streak along the streamwise direction and the subsequent exposure of the particles to an almost constant mean gas velocity.

Phase-average measurements of the fluctuating gas velocity–attenuation product, $u_g \xi$, are presented in figure 32. In order to help in interpreting them, these ϕ–y surfaces display cross-stream positions located only between $-50.8 \leqslant y \leqslant -15.9$ mm. The y-position of the cut corresponds, approximately, to their plane of symmetry. The orientation of the phase axis is identical to that of figure 27.

The $u_g \xi$ surfaces are characterized by two prominent negative regions. The first one, the left of the graph, is the result of the product of positive fluctuating attenuations (streak's emergence) and negative fluctuating velocities (vortices' braid). The second one is created by the product of negative attenuation fluctuating values (depletion area) and positive fluctuating longitudinal velocities (vortices' core). Notice that at $x = 10.2$ cm, the peak corresponding to the braid is smaller than the one in the core, indicating the still relatively weak dispersion activity and the strong coherent correlation of the velocity signal. This situation is reversed at $x = 20.3$ cm, as the braid negative region becomes more pronounced than the core negative peak, showing the increase in particle dispersion activity and the decrease in the coherency of the velocity fluctuating signal.

The phase-average measurements performed with the particle sizer are shown in figure 33. At every downstream location the figures simultaneously display the overall particle concentration and the Sauter mean diameter of the distribution. Unlike in the attenuation measurements, the raw data have been smoothed out and the surfaces have been presented with a resolution two times greater than that of the original data. Care was taken to ensure that the smoothing routine generated an approximating surface located within 2% of the original data.

The general conclusions obtained from the attenuation measurements are found to be consistent with the trends appearing in the concentration surfaces. The shape of the streaks and the engulfed depletion region are defined at $x = 15.2$ cm. Comparison between the concentration and SMD surfaces reveals that the depletion hole is characterized by small values of the mean diameter. As a result, the concentration values associated with this region are smaller than the corresponding attenuation levels. For $x = 20.3$ cm, the concentration in the depletion area is only 4% of the free-stream value, whereas the streak centreline is characterized, for the same phase coordinate, by concentration levels close to 20% that of the free-stream value. Notice that the streak emergence point is characterized by a depression in the local concentration level, indicating the strong particle cross-stream velocity gradients existing in this region. The progressive accumulation of droplets occurring in the core of the spray facing the depletion area is also evident in figure 33, being quite prominent at $x = 20.3$ cm.

In between depletion areas, the SMD reaches a maximum value in the region close to the streak centreline. The surface plots, however, show the existence of a relative shift between the locations where the concentration and SMD achieve their respective higher levels. Specifically, the locus of the maxima in the mean diameter is displaced towards the vortex periphery with respect to the location of the maximum concentration (streak centreline). This effect can be more clearly observed in figure 34, showing the phase dependence of the concentration and SMD for two

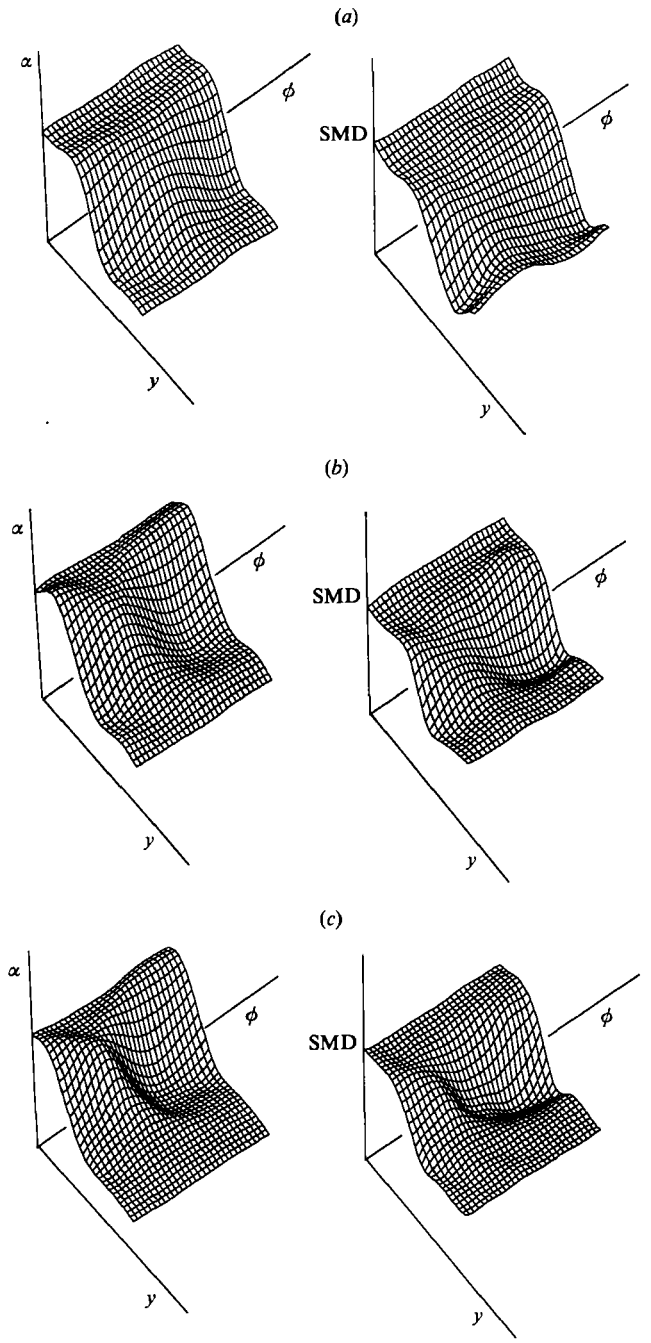

FIGURE 33. Overall particle concentration and Sauter mean diameter phase-average measurements. The surfaces display the particle field magnitudes as a function of the cross-stream coordinate and the phase value. (*a*) $x = 10.2$ cm; (*b*) 15.2 cm; (*c*) 20.3 cm.

different values of the cross-stream coordinates that intersect both the streak emergence and the depletion region. In order to show the effectiveness of the smoothing routine, both the raw data and the smoothed surface have been presented in the figure.

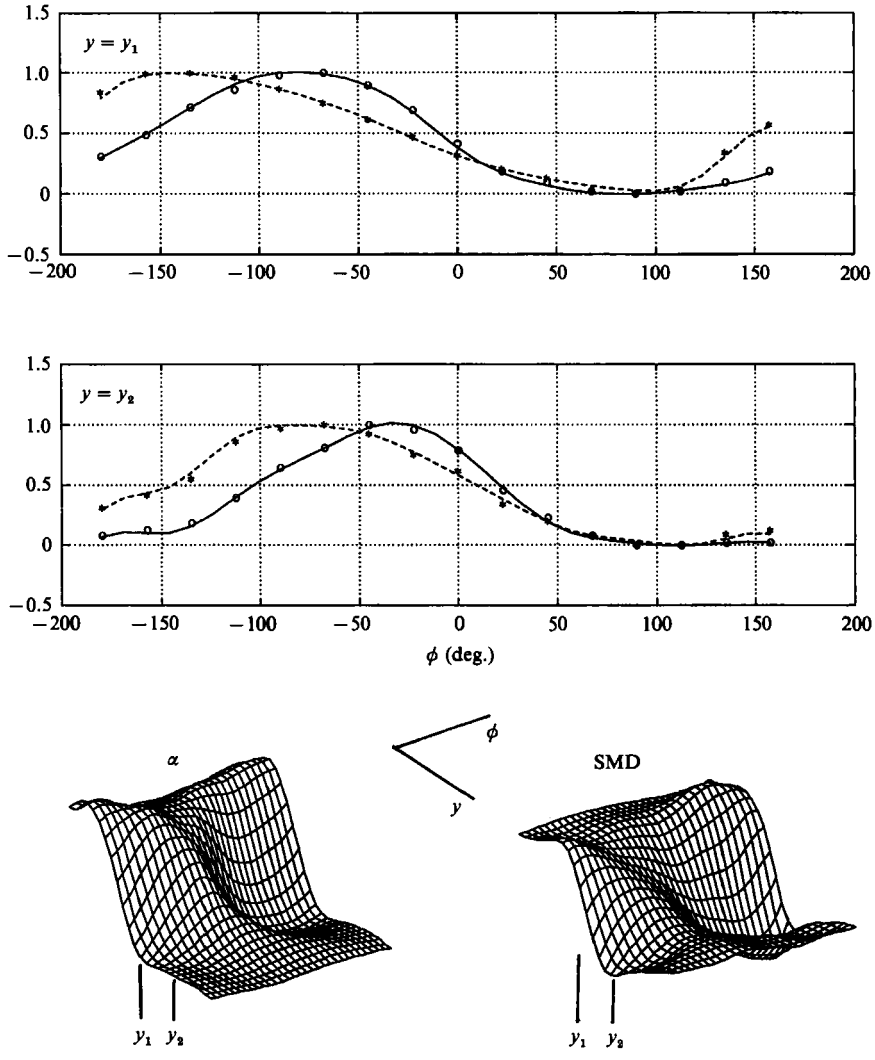

FIGURE 34. ○, Normalized overall particle concentration $(\alpha-\alpha_{min})(\alpha_{max}-\alpha_{min})$; and *, $(SMD-SMD_{min})/(SMD_{max}-SMD_{min})$ variation with the forcing phase, $x = 15.2$ cm. Cross-stream coordinate is placed in the streak emergence region.

Notice that although the minimum locations for both concentration and SMD are located at the same phase point, there is a shift between the phase value at which the maximum in the concentration and mean diameter are reached. As already mentioned, the SMD peaks farther away from the vortex core than the concentration does. Observe also that the amount of phase shift decreases with y.

At the leading edge of the dispersion structure (figure 35), the SMD is seen to increase monotonically from the small values found at the depletion hole. Thus, it can be noticed that the mean diameter is still increasing at cross-stream positions higher than the ones for which the concentration reaches its local, streak-associated maximum.

The above observations can be understood by analysing the response of the different droplet family groups to the velocity field induced by the vortices. In particular, the non-dimensionalization arguments presented in §5 suggest that the

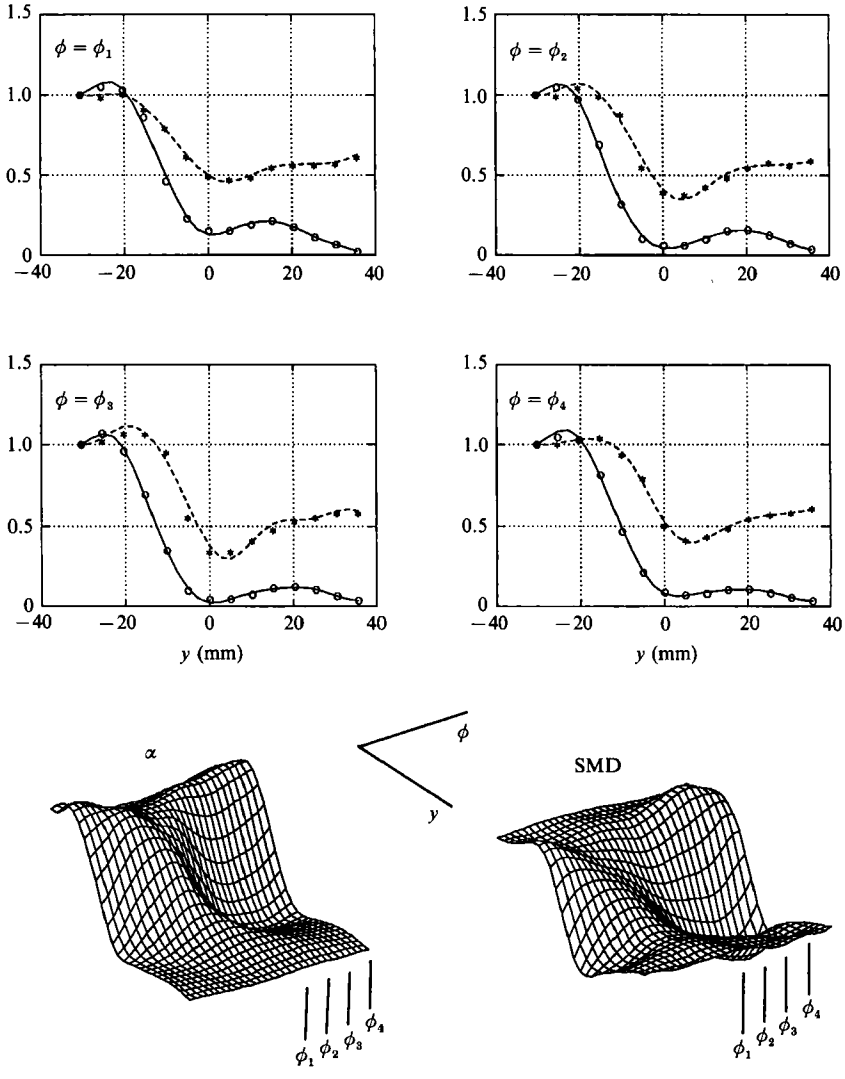

FIGURE 35. ○, Normalized overall particle concentration (α/α_∞) and SMD (SMD/SMD_∞) variation with the cross-stream coordinate, $x = 15.2$ cm. Forcing phase value is selected in the streak leading-edge region.

characteristic length of the dispersion associated with the large scale should be proportional to the particle diameter. We should expect, therefore, spatial shifts in the streak centrelines describing the dispersion of the different diameters. The emergence point of the large sizes, consequently, should be located farther away from the vortex core than those characterizing the smaller diameter groups. In addition, the polar extension of the particle dispersion process is also dependent upon the size. The polar angle can be expressed as the ratio between two rectangular coordinates and, therefore, does not require non-dimensionalization. Its size dependence, however, enters through the temporal variable, which scales with a magnitude that is proportional to the square of the particle diameter.

In conclusion, at a given downstream distance, the large-scale dispersion must have streaks characterized by emergence points separated from the vortex core at a

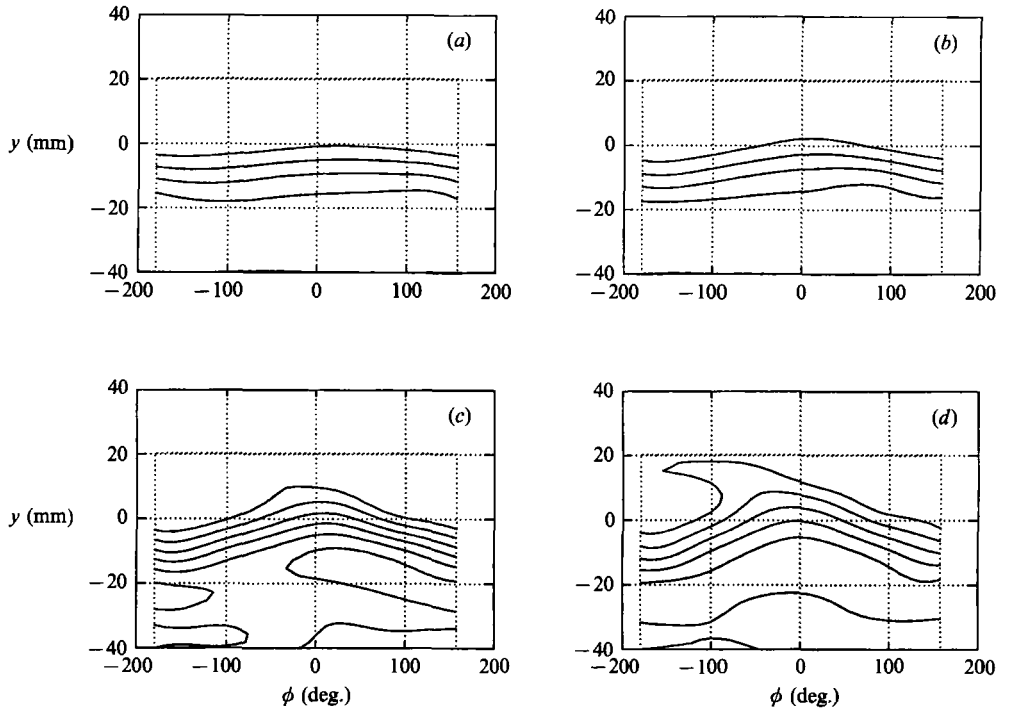

FIGURE 36. Phase average measurements of the particle concentration for four different particle size groups. $x = 10.2$ cm. Isocontour levels correspond to 0.2, 0.4, ..., 1.2 times the unperturbed concentration value. (*a*) $\bar{D} = 74.5$ μm, (*b*) 44.6 μm, (*c*) 27.0 μm, (*d*) 16.5 μm.

distance which increases with the size and that displays a higher polar development for the small droplets. When the particles are subjected not to one simple vortex, but to a row of consecutive vortices, these conclusions, to a first approximation, should still be true. However, since the range of influence of a particular vortex is now reduced to separations from its core within $\pm\frac{1}{2}\lambda$ (with λ being the wavelength of the vortices' row), we have to expect a less pronounced streak emergence point dependence on the particle size.

These observations are consistent with the phase-average concentration measurements performed for the different droplet diameters. Figures 36–38 present the isocontour plots of the concentration ϕ–y surfaces for four different particle groups, characterized by central diameters $\bar{D} = 74.5$, 44.6, 27.0 and 16.5 μm. Fixing the x-coordinate is similar to analysing the streak structures at a given time after the beginning of the dispersion. For a given downstream location, the streak emergence point and the polar development dependence on the particle size are evident. Compare at $x = 20.3$ cm (figure 38) the difference in phase location of the streak emergence point for $\bar{D} = 16.5$ μm and $\bar{D} = 74.5$ μm. Notice how, for the large diameter, the streak emerges farther away from the core of the depletion area. There are also indications that the phase shift existing in the emergence region between different particle sizes is increasing with the downstream location. The contour plot tangent to $y = 0$ mm shows a phase difference of about 30° between $\bar{D}_1 = 16.5$ μm and $\bar{D}_2 = 75.5$ μm at $x = 10.2$ cm. For $x = 20.3$ cm this difference becomes 45°.

The downstream dependence of the phase shift reveals the existence of relative longitudinal motions between different particle sizes, and indicates that the particles

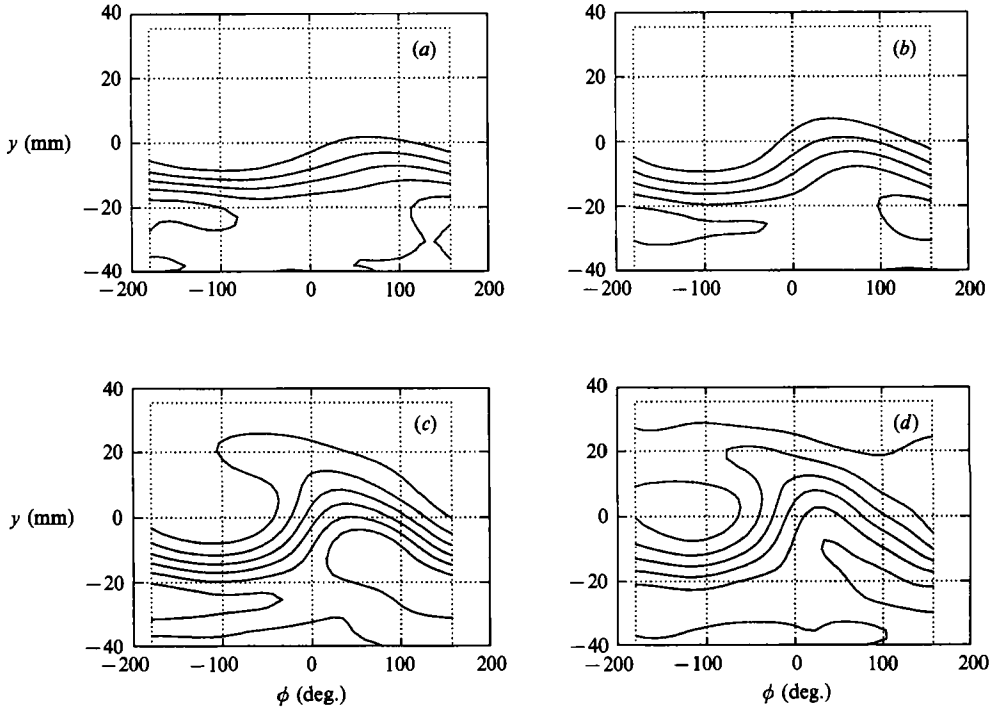

FIGURE 37. As figure 36 but at $x = 15.2$ cm.

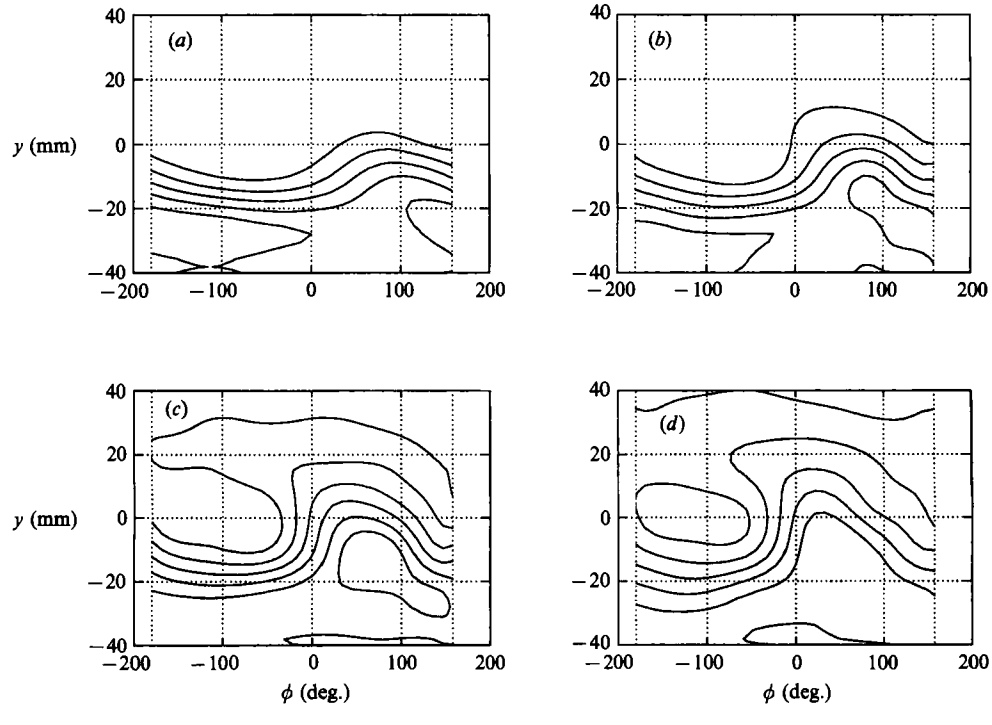

FIGURE 38. As figure 36 but at $x = 20.3$ cm.

in the dispersion layer still possess some residual extra longitudinal velocity from the region where they were generated (core of the spray). Furthermore, this residual velocity increases with the diameter. These observations are in agreement with previous LDV measurements of the mean velocity field performed in a plane mixing layer seeded with variable-size particles (Crowe *et al.* 1988).

Notice also that this slip effect is consistent with the downstream shift observed in the time delay necessary to achieve the gas velocity–attenuation cross-correlation maxima (figure 25).

The polar development of the evolution is also seen to strongly depend on the particle size. Compare, for example, the more external isocontour line (corresponding to a particle group concentration equal to 0.2 of the free-stream value) and notice, for different size groups, the large differences in the polar angle swept from its leading edge to the streak emergence region.

Keeping in mind the radial and polar dependence that the large-scale dispersion exhibits with respect to the particle size, the experimental evidence presented here is then understood. The shift towards the vortex periphery that the SMD peak has with respect to the concentration maxima now becomes clear. Also, analysing more external cross-stream positions corresponds to an increase in the polar coordinate with respect to the vortex core. As a result, the maximum particle diameter present in the dispersion structure decreases when increasing the cross-stream coordinate. It follows that the phase separation between the maxima points in the SMD and overall concentration profiles must become smaller; this is consistent with the results shown in figure 34. Finally, the mechanism presented in figure 20 for the stabilization in the particle distribution indicators (such as the SMD) via the streak interconnection event is also confirmed. For cross-stream coordinates wet by both ascending and descending branches of the dispersion streak, the relative contribution of both portions towards the measured indicator compensate each other when comparing two different cross-stream locations. As a consequence, a plateau in the cross-stream profile is obtained.

8. Eulerian modelling of the large-scale particle dispersion

The continuum formulation approach of the particle dispersion problem (Drew 1983) is especially attractive when the gas motion is two-dimensional and is characterized by localized concentrations of vorticity separated by extensive areas of an almost irrotational flow. Under these conditions it can be demonstrated that if the continuum particle velocity field originates as an irrotational motion, the particle flow will be irrotational everywhere (Robinson 1956), with the consequent simplification in the flow description. In the developing forced mixing layer, the rapid growth of the Kelvin–Helmholtz instability quickly leads to the concentration of the vorticity shed from the splitter plate in the regions defining the spanwise vortices' cores. In this case, therefore, the mixing layer is composed of extensive areas of almost irrotational motion. As a consequence and, outside of the vortices' cores, the particle velocity will be irrotational, with the subsequent simplification in the continuum flow description. The usefulness of the continuum approach in these cases will be explored here by considering the motion of the particles in a simplified gas flow represented by a potential point vortex characterized by a circulation Γ. This simplified model should represent the physical situation encountered by the small particles in their initial dispersion since, in this case, the particles remain within the region of influence of the vortex in which they originally disperse. The

continuum equations governing the motion of a dilute spray composed by small, heavy particles which remain outside the vortex viscous core are then given by

$$\frac{\partial \boldsymbol{u}_{\mathrm{p}}}{\partial t}+\boldsymbol{u}_{\mathrm{p}}\cdot\nabla\boldsymbol{u}_{\mathrm{p}}=\frac{\boldsymbol{e}_{\theta}}{2\pi r}-\boldsymbol{u}_{\mathrm{p}} \quad \forall r > r_{\mathrm{c}}\left(\frac{\bar{u}_{\mathrm{g}\infty}}{\Gamma L_{D}}\right)^{\frac{1}{2}}, \tag{11}$$

$$\frac{\partial \alpha_{\mathrm{p}}}{\partial t}+\nabla\cdot(\alpha_{\mathrm{p}}\boldsymbol{u}_{\mathrm{p}})=0. \tag{12}$$

Here, we have used a polar coordinate system centred at the vortex and the non-dimensionalization given by (2).

The forcing term in the particle velocity equation does not depend on the polar angle θ. If, in addition, the initial condition for the particles' velocity possesses axisymmetry, we seek the solution of (11) such that

$$\partial \boldsymbol{u}_{\mathrm{p}}/\partial\theta=\boldsymbol{0} \quad \forall t\geqslant 0. \tag{13}$$

Furthermore, if we assume that the particle velocity is irrotational at $t=0$, it implies that

$$\omega_{z\mathrm{p}}=\frac{\partial}{\partial r}(ru_{\mathrm{p}_{\theta}})=0 \quad \forall r > r_{\mathrm{c}}\left(\frac{\bar{u}_{\mathrm{g}\infty}}{\Gamma L_{D}}\right)^{\frac{1}{2}} \forall t\geqslant 0. \tag{14}$$

Integration of (14) gives

$$u_{\mathrm{p}_{\theta}}=k(t)/2\pi r. \tag{15}$$

The velocity equations then become, with the axisymmetric condition (13):

$$\frac{\partial u_{\mathrm{p}_r}}{\partial t}+u_{\mathrm{p}_r}\frac{\partial u_{\mathrm{p}_r}}{\partial r}+u_{\mathrm{p}_r}=\frac{u_{\mathrm{p}_{\theta}}^{2}}{r}, \tag{16}$$

$$\frac{\partial u_{\mathrm{p}_{\theta}}}{\partial t}+u_{\mathrm{p}_r}\frac{\partial u_{\mathrm{p}_{\theta}}}{\partial r}+\frac{u_{\mathrm{p}_r}u_{\mathrm{p}_{\theta}}}{r}+u_{\mathrm{p}_{\theta}}=\frac{1}{2\pi r}. \tag{17}$$

For the polar particle velocity field given by (15), the nonlinear terms in the polar momentum conservation equation vanish identically. Therefore (17) can be integrated to give

$$u_{\mathrm{p}_{\theta}}(r,t)=\frac{1+A\,\mathrm{e}^{-t}}{2\pi r}. \tag{18}$$

The general initial condition for an axisymmetric, irrotational particle velocity field is that in which the particles possess some initial circulation Γ_{p_0}:

$$u_{\mathrm{p}_{\theta}}(0,r)=\frac{\Gamma_{\mathrm{p}_0}}{2\pi r} \quad \forall r > r_{\mathrm{c}}\left(\frac{\bar{u}_{\mathrm{g}\infty}}{\Gamma L_{D}}\right)^{\frac{1}{2}}. \tag{19}$$

The solution for the polar component of the particle velocity field is then

$$u_{\mathrm{p}_{\theta}}=\frac{1+(\Gamma_{\mathrm{p}_0}-1)\,\mathrm{e}^{-t}}{2\pi r}. \tag{20}$$

In particular, if the particles have initially the same velocity as the gas, $\Gamma_{\mathrm{p}_0}=1$, whereas if the particles are initially at rest $\Gamma_{\mathrm{p}_0}=0$.

The evolution of the radial velocity field is given by introducing (20) into (16):

$$\frac{\partial u_{\mathrm{p}_r}}{\partial t}+u_{\mathrm{p}_r}\frac{\partial u_{\mathrm{p}_r}}{\partial r}+u_{\mathrm{p}_r}=\frac{(1+(\Gamma_{\mathrm{p}_0}-1)\,\mathrm{e}^{-t})^{2}}{4\pi^{2}r^{3}}, \tag{21}$$

and this nonlinear equation must be solved numerically.

For large values of r, however, the equation can be approximated by

$$\frac{\partial u_{p_r}}{\partial t} + u_{p_r} = \frac{(1 + (\Gamma_{p_0} - 1)\,e^{-t})^2}{4\pi^2 r^3}. \tag{22}$$

For $r \leqslant o(1)$ and with an initial zero particle–gas relative velocity, the unsteady term, $\partial u_{p_r}/\partial t$, is the leading effect in the first steps of the dispersion process, $t \ll r^2$. For $t = o(r^2)$ the nonlinear term is of the same order of magnitude as the unsteady effect, tending to further increase the radial particle velocity. The radial motion depletes the central vortex core from particles and it takes $t = o(r^2)$ until the depletion reaches the position r. Therefore, for a given radial position, there is a time interval for which the approximation (22) is not valid. For particles initially at rest, the time necessary for the nonlinear effects to be of the same order of magnitude as the unsteady term is $t = o(r)$, which is also the time that it takes the depleted area to reach the position r.

Since the characteristic length in the non-dimensionalization (2) scales proportionally with the particle diameter, the regions of the flow field for which (22) gives adequate results increase for decreasing particle sizes.

For $u_{p_r}(0, r) = 0$ the solution of the linearized equation is given by

$$u_{p_r} = \frac{\int_0^t (1 + (\Gamma_{p_0} - 1)\,e^{-t})^2\, e^{-(t-\tau)}\,d\tau}{4\pi^2 r^3}. \tag{23}$$

For particles initially at rest, $\Gamma_{p_0} = 0$, the result is

$$u_{p_r} = \frac{1 - 2t\,e^{-t} - e^{-2t}}{4\pi^2 r^3}, \tag{24}$$

whereas for particles initially moving at the same velocity as the gas, $\Gamma_{p_0} = 1$:

$$u_{p_r} = \frac{1 - e^{-t}}{4\pi^2 r^3}. \tag{25}$$

The evolution of the concentration field can be obtained, in both cases, by integrating (12):

$$\partial\alpha/\partial t + 1/r\,\partial/\partial r(r u_{p_r}\alpha) + 1/r\,\partial/\partial\theta(u_{p_\theta}\alpha) = 0. \tag{26}$$

Introducing into (26) the expressions for the particle velocity field for the case in which the particles move initially with the gas, the result is

$$2\pi r^2 \frac{\partial\chi}{\partial t} + \frac{1 - e^{-t}}{2\pi r}\frac{\partial\chi}{\partial r} + \frac{\partial\chi}{\partial\theta} = 0, \tag{27}$$

with

$$\chi = \alpha/r^2. \tag{28}$$

The characteristics of (27) are given by

$$\frac{dt}{2\pi r^2} = \frac{2\pi r\,dr}{1 - e^{-t}} = \frac{d\theta}{1}, \tag{29}$$

which integrate to

$$r = (r_0^4 + 1/\pi^2(t - (1 - e^{-t})))^{\frac{1}{4}}, \tag{30}$$

$$\theta = \theta_0 + \int_0^t \frac{d\tau}{2\pi\{r_0^4 + (1/\pi^2)(\tau - (1 - e^{-\tau}))\}^{\frac{1}{2}}}. \tag{31}$$

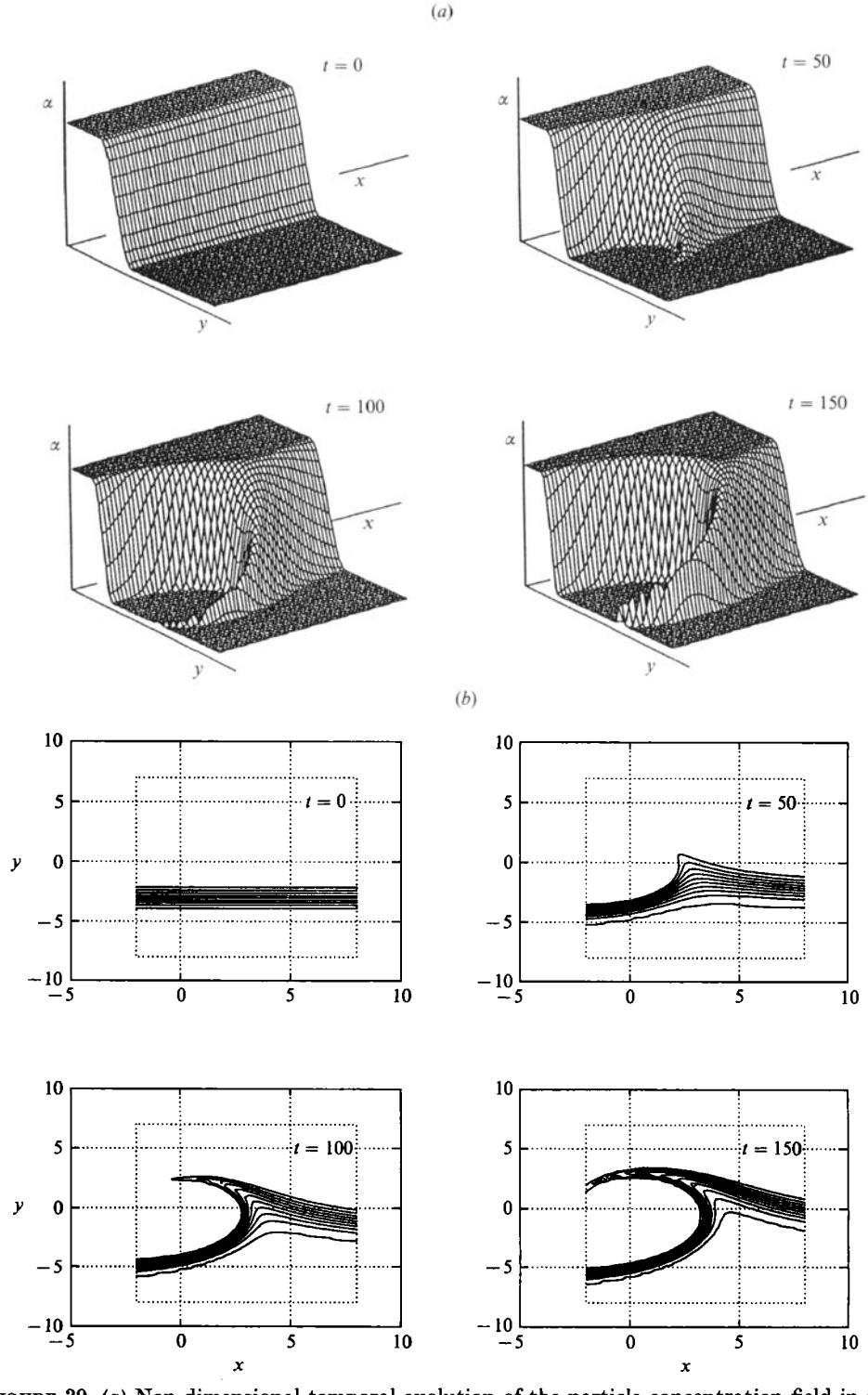

FIGURE 39. (*a*) Non-dimensional temporal evolution of the particle concentration field in a point vortex. Particles initially located in a half-plane with respect to the vortex and moving with the gas. (*b*) Non-dimensional temporal evolution of the particle concentration field in a point vortex. Isocontour plots of (*a*). Non-dimensional concentration levels at 0.1, 0.2, ..., 1.2.

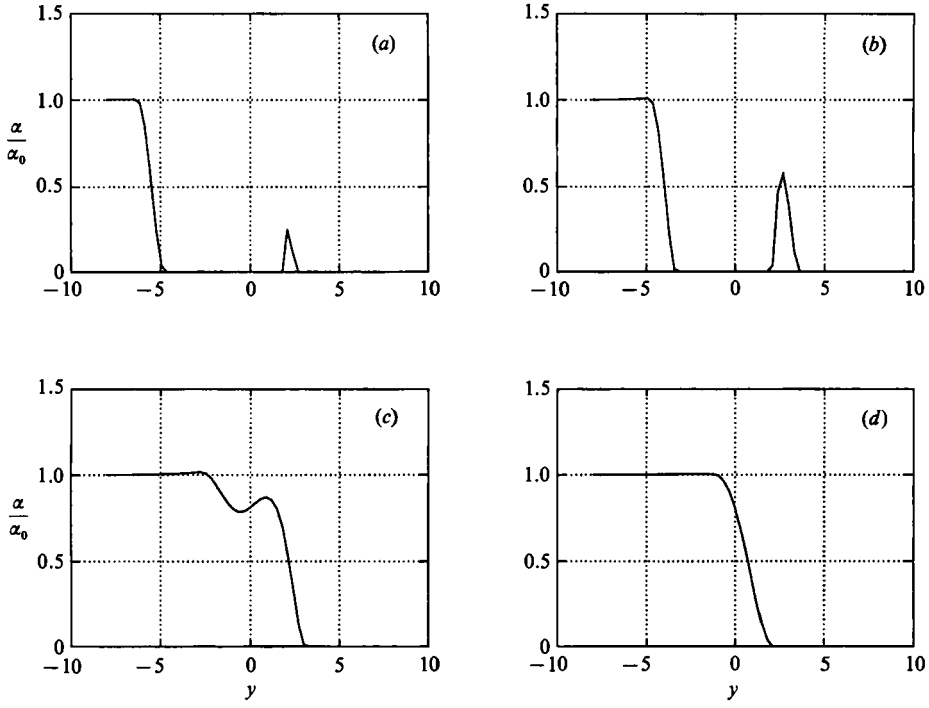

FIGURE 40. Particle concentration field in a point vortex. Non-dimensional time $t = 150$. Curves represent x = constant cuts of the $t = 150$ surface presented in figure 39(*a*). (*a*) $x = -1.6$, (*b*) $x = 2$, (*c*) $x = 4$, (*d*) $x = 6$.

For large values of t, (30) and (31) give the correct asymptotic trend for particles evolving in a point vortex (Lázaro & Lasheras 1989)

$$r \propto t^{\frac{1}{4}}, \tag{32}$$

$$\theta \propto t^{\frac{1}{2}}, \tag{33}$$

indicating that for large values of t, the polar rollup occurs at a faster rate than the radial depletion.

For arbitrary times, (30) and (31) can be used to determine the concentration field in the (r, θ)-plane. The concentration at a point r, θ is obtained by calculating the initial point r_0, θ_0 at time $t = 0$ of the characteristic that passes over r, θ at time t. The concentration at r, θ is then given by

$$\alpha(r, \theta, t) = \alpha(r_0, \theta_0, 0)\, r^2/r_0^2. \tag{34}$$

The system given by (30), (31) and (34) has been solved numerically and the results are given in figures 39 and 40. To avoid the vortex viscous core and the conflict existing for $r \leqslant 1$ the particles are initially located at $y \leqslant -1.5$. To simulate the concentration boundary layer, the initial concentration field is given by

$$\alpha(x, y, 0) = \begin{cases} 0, & y \geqslant -1.5, \\ \sin^2(\frac{1}{6}\pi(y+1.5)), & -4.5 \leqslant y < -1.5, \\ 1, & y < -4.5. \end{cases} \tag{35}$$

Therefore, the 0–99 % level concentration boundary-layer thickness is set equal to 3 non-dimensional lengths. Since the characteristic length for particles $D = 5$ μm is about 1 cm (equation (2)), the present simulations should reproduce the experimental

conditions for that diameter range. In this case, the maximum non-dimensional time displayed, $t = 150$, corresponds to 12 ms or about 10 cm from the end of the splitter plate.

The hyperbolic character of (11) and the irrotationality of the particle motion result in a tendency to form strong conventration gradients as the dispersion proceeds. This tendency, which has been used to create singular points of high particle concentration in aerosol flows (Fernández de la Mora & Riesco-Chueca 1988), in our case produces an accumulation of material around the inner edge of the depletion region, leading to steeper boundary-layer concentration profiles in those areas. Figure 40 shows several x = constant profiles of the particle concentration surface at time $t = 150$. Note the close resemblance of the shapes of the concentration profiles shown in figure 39 with the experimental measurements given in figures 27 and 28. As was the case with the experimental data, the model shows the existence of an inner zone depleted of particles and two sublayers where the accumulation of droplets occurs. In the positions corresponding to the braids connecting consecutive dispersion structures (figure 39*d*) the concentration profile shows a single inflexion point. However, the centres of the dispersion structure (figure 39*a–c*) exhibit profiles having two maxima, in agreement with the experimental evidence presented in figure 29.

9. Conclusions

We have presented an experimental study of the dispersion of small, heavy particles in the developing region of an acoustically excited plane gaseous mixing layer. It has been shown that the particle concentration field is characterized by a degree of coherency and activity much higher than the one found in the naturally developing flow. The instantaneous particle dispersion field was found to be composed of large, equally spaced streaks that engulf extensive areas of very small particle concentration values. Velocity–concentration cross-correlation measurements showed that this depletion region is located in the core of the large-scale vortical structures that dominate the evolution of the gaseous flow. As with the naturally developing dispersion layer, the mean-particle concentration field was also found to be characterized by an initial induction region. However, the asymptotic state was found now to exhibit a higher spreading rate than that of the gas flow momentum.

Owing to the lack of self-similarity in the base-flow momentum and the existence of a higher mixing activity, the particle dispersion field was found not to possess a universal, diameter-independent behaviour.

Conditional measurements showed strong irregularities not only in the concentration field, but also in the mean diameters of the distribution. The depletion area was shown to be characterized by the presence of very small droplets whereas local accumulation of large droplets occurred in the streak's periphery. The phase-conditioned measurements also revealed the increasing extension of the induction region with the particle diameter. The distance between the vortex's core and the streak's emergence point was also found to be dependent on the particle diameter, increasing with it.

Finally, particle dispersion modelling in an isolated point vortex was conducted in an Eulerian framework. This simplified flow model produced a good qualitative agreement with the experiments, indicating that the initial stages of the particle dispersion process can be qualitatively understood with simple dynamic arguments.

REFERENCES

ANTONIA, R. A. 1983 Conditional sampling in turbulence measurement. *Ann. Rev. Fluid Mech.* **13**, 131–156.

BROWAND, F. K. & WEIDMAN, P. D. 1976 Large scales in the developing mixing layer. *J. Fluid Mech.* **76**, 127–144.

BROWN, G. L. & ROSHKO, A. 1974 On density effects and large structure in turbulent mixing layers. *J. Fluid Mech.* **64**, 775–816.

CHEIN, R. & CHUNG, J. N. 1988 Simulation of particle dispersion in a two-dimensional mixing layer. *AIChE J.* **34**, 946–954.

CHUNG, J. N. & TROUTT, T. R. 1988 Simulation of particle dispersion in an axisymmetric jet. *J. Fluid Mech.* **186**, 199–222.

CROWE, C. T., CHUNG, J. N. & TROUTT, T. R. 1988 Particle mixing in free shear flows. *Prog. Energy Combust. Sci.* **14**, 171–194.

DREW, D. A. 1983 Mathematical modelling of two-phase flows. *Ann. Rev. Fluid Mech.* **15**, 261–291.

FERNÁNDEZ DE LA MORA, J. & RIESCO-CHUECA, P. 1988 Aerodynamic focusing of particles in a carrier gas. *J. Fluid Mech.* **195**, 1–21.

FIEDLER, H. E. & MENSING, P. 1985 The plane turbulent shear layer with periodic excitation. *J. Fluid Mech.* **150**, 281–309.

FREYMUTH, P. 1966 On transition in a separated laminar boundary layer. *J. Fluid Mech.* **25**, 683–704.

HO, C. K. & HUANG, L. S. 1982 Subharmonic and vortex merging in mixing layers. *J. Fluid Mech.* **119**, 443–473.

LÁZARO, B. J. 1989 Particle dispersion in turbulent free shear flows. Ph.D. dissertation, University of Southern California.

LÁZARO, B. J. & LASHERAS, J. C. 1989 Particle dispersion in a turbulent, plane, free shear layer. *Phys. Fluids* A **1**, 1035–1044.

LÁZARO, B. J. & LASHERAS, J. C. 1992 Particle dispersion in the developing free shear layer. Part 1. The natural flow. *J. Fluid Mech.* **235**, 143–178.

ROBINSON, A. 1956 On the motion of small particles in a potential field of flow. *Commun. Pure Appl. Maths.* **IX**, 69–84.

WYGNANSKI, I., OSTER, D. & FIEDLER, H. A. 1979 A forced plane, turbulent mixing layer: a challenge for the predictor. In *Turbulent Shear Flows 2*, pp. 314–326. Springer.